Microstructural Design of Fiber Composites

Tsu-Wei Chou

Book DOI: http://dx.doi.org/10.1017/CBO9780511600272

Online ISBN: 9780511600272

Hardback ISBN: 9780521354820

Paperback ISBN: 9780521019651

Chapter

7 - Three-dimensional textile structural composites pp. 374-442

Chapter DOI: http://dx.doi.org/10.1017/CBO9780511600272.008

Cambridge University Press

7 Three-dimensional textile structural composites

7.1 Introduction

Three-dimensional textile preforms are fully integrated continuous-fiber assemblies with multi-axial in-plane and out-of-plane fiber orientations (Chou, McCullough and Pipes 1986; Ko 1989a). Composites reinforced with three-dimensional preforms exhibit several distinct advantages which are not realized in traditional laminates. First, because of the out-of-plane orientation of some fibers, three-dimensional preforms provide enhanced stiffness and strength in the thickness direction. Second, the fully integrated nature of fiber arrangement in three-dimensional preforms eliminates the inter-laminar surfaces characteristic of laminated composites. The superior damage tolerance of three-dimensional textile composites based upon polymer, metal and ceramic matrices has been demonstrated in impact and fracture resistance. Third, the technology of textile preforming provides the unique opportunity of near-net-shape design and manufacturing of composite components and, hence, minimizes the need for cutting and joining the parts. The potential of reducing manufacturing costs for special applications is high. The overall challenges and opportunities in three-dimensional textile structural composites are very fascinating.

Three-dimensional textile preforms can be categorized according to their manufacturing techniques. These include braiding, weaving, knitting and stitching, as shown in Fig. 7.1.

There are three basic braiding techniques for forming three-dimensional preforms, namely 2-step, 4-step and solid braidings. In the case of 2-step braiding, the axial yarns are stationary and the braider yarns move among the axials. Thus, the axial yarns are responsible for the high stiffness and strength in the longitudinal direction and relatively low Poisson contraction. A high degree of flexibility in manufacturing can be achieved in 2-step braiding by varying the material and geometric parameters of the axial and braider yarns.

Flexibility in the manufacturing of 4-step braids is somewhat less than that of 2-step braids. All yarn carriers change their positions in the braiding process and do not maintain a straight

configuration. As a result, the preforms exhibit relatively high Poisson contractions. In order to enhance the longitudinal stiffness and strength, straight laid-in yarns are often employed.

It can be demonstrated that 4-step and 2-step braidings are merely variations of a general braiding scheme. By inserting some axial yarns and placing braiding yarns at proper locations on the braiding machine, a 4-step braiding process can be converted to a 2-step braiding process.

Besides the more recently developed 2-step and 4-step braidings, which involve the sequential and discrete movement of yarn carriers, the maypole type braiding technique is also capable of producing three-dimensional solid braids. Both square and circular shapes are feasible. The technology of solid braiding has been well developed, and commercial machines are available with the maximum number of carriers currently limited to 24. The application of solid braids to composite materials is limited to simple shapes.

In woven preforms, there are two major categories. The angle-interlock multi-layer weaving technique requires interlacing the yarns in three dimensions. The warp yarn in this three-dimensional construction penetrates several weft layers in the thickness direction, and therefore the preform structure is highly integrated. In orthogonal wovens, the yarns assume three mutually perpendicular orientations in either a Cartesian coordinate system or a cylindrical coordinate system. The yarns in the Cartesian weave are not wavy, and as a result matrix rich regions often appear in the composites.

The process of stitching is mainly based upon an existing technology for converting two-dimensional preforms to three-dimensional ones. Because of the simplicity of the stitching operation, it is feasible to join composite parts continuously in a cost-effective manner. Both lock stitch and chain stitch have been

Fig. 7.1. Three-dimensional textile preforms.

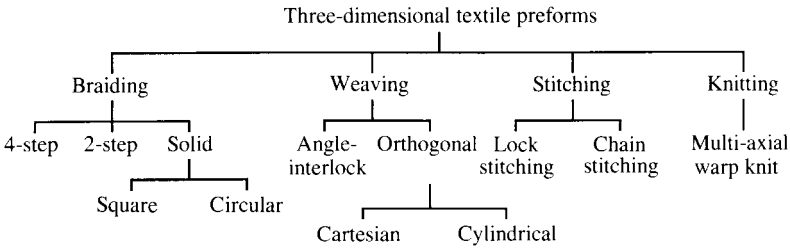

utilized. Major concerns of the stitching operation include depth of penetration of the stitching yarns and, hence, the thickness of two-dimensional preforms that can be stitch-bonded, as well as the degree of sacrifice of the in-plane properties due to the damage to in-plane yarns.

The technique of knitting is particularly desirable for producing preforms with complex shapes because the variability of the geometric forms is almost unlimited. The large extensibility and conformability of the preforms enable them to be designed and manufactured for reinforcing composites subject to complex loading conditions. The versatility of knitted preforms offers a new dimension in textile structural composites technology.

In this chapter the discussion of knitting is focussed on the conversion of two-dimensional structures (for example, unidirectional laminae) to three-dimensional ones through knit-loop-bonding. In this process, the two-dimensional layers or structures are formed at the same time when they are bonded. The technology of multi-directional multi-layer warp knit, for instance, is attractive because it enables the bonding of the unidirectional lamina by knitting yarns whereas the yarns in an individual lamina remain straight. In other words, unlike the stitch-bond of woven fabrics, the yarns in the two-dimensional structure are not wavy and hence do not sacrifice their stiffness and strength in the principal material directions. The manufacturing process is highly integrated, and the properties in the through-the-thickness direction depend upon the density and material of the knitting yarn. The potential of knitting in producing cost-effective thick laminates is attractive.

7.2 Processing of textile preforms

This section outlines the processing techniques of braiding, weaving, stitching and knitting for making three-dimensional textile preforms, with particular emphasis on braiding and weaving. According to Du, Popper and Chou (1991), braiding can form shapes either by overbraiding mandrels in conventional circular machines or by using new braiding patterns to form solid shapes directly. Weaving can be done by using either conventional looms with multi-layer constructions or entirely new equipment. Knitting can be used to interconnect fiber arrays that have been arranged by other techniques. Stitching has been used to interconnect layers of two-dimensional fabrics for achieving desired thickness and inter-laminar strength.

7.2.1 *Braiding*

Three-dimensional braids have been produced on traditional horn-gear machines. At the present time, horn-gear based braiding machines use a small number of yarn carriers ($\leq$24) and cannot form complex shapes. Their applicability is therefore limited. A number of new machines have been developed to create complex shapes. These newer braiding processes include 2-step (Popper and McConnell 1988), AYPEX (Weller 1985), interlock twiner (Cole 1988), and row and column (Florentine 1982), which is also referred as *Omniweave, Magnaweave*, or *4-step* in the literature.

A schematic view of a set-up for the three-dimensional braiding process is shown in Fig. 7.2. Axial yarns, if present in a particular braid, are fed directly into the structure from packages located below the track plate. Braiding yarns are fed from bobbins mounted on carriers that move on the track plate. The pattern of motion of the braiders and the presence/absence of axial yarns determine the type of braids, as well as the microstructure. The processes of 2-step and 4-step braiding are introduced below.

7.2.1.1 *2-step braiding*

The preform structure of a 2-step braid includes a large number of parallel (axial) yarns aligned for efficient reinforcement and a smaller number of braiding yarns (braiders) that interconnect

Fig. 7.2. A set-up for three-dimensional braiding. (After Du, Popper and Chou 1991.)

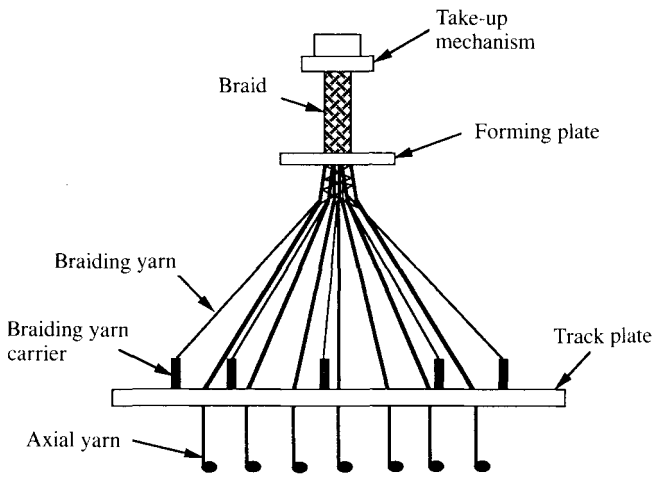

the axial yarns and form the fabric shape. The axial array can be arranged in essentially any shape, including I-beams, box beams, circular tubes, etc., whereas the braiders are arranged around the perimeter of the axial array as shown in Fig. 7.3. In the braiding process, the braiders move through the axial array in two sequential steps. In the first, the braiders all move in one diagonal line but in alternating directions (Fig. 7.3a). In the second, they move along the other diagonal line (Fig. 7.3b).

Although the machine action consists of only two steps, each braider moves through a larger portion of the structure. This can be seen by tracing the path of a single braider subjected to the repeated 2-step machine action. The paths followed by all braiders will completely intercinch the axial yarns and lock them in the desired shape.

Compared with other three-dimensional braiding processes, 2-step braiding has several distinct advantages. A relatively simple sequence of braider motions can form a wide range of shapes. During each step of the process, all the braiders are simultaneously outside of the axial array, and thus it is possible to add various inserts to the structure or even rearrange the axial array geometry to change the preform cross-section. Furthermore, this structure can be made with a high level of fiber packing and a large number of axially oriented fibers as needed in many applications (Du, Popper and Chou 1989, 1991).

The 2-step process has motivated a number of researchers. Li and El Shiekh (1988) modeled the microgeometry using idealized

Fig. 7.3. 2-Step braiding pattern showing the relative motion of yarns. (After Du, Popper and Chou 1991.)

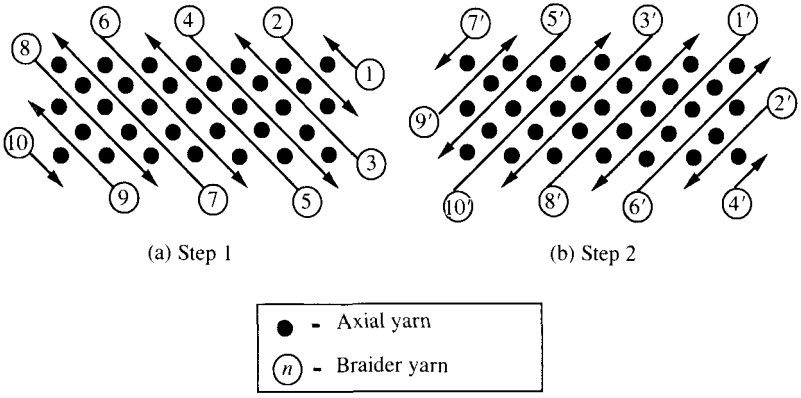

circular yarns. Ko, Soebroto and Lei (1988) and Whitney (1988) have evaluated the mechanical properties of consolidated 2-step composites.

7.2.1.2 *4-step braiding*

The 4-step braiding process, so named by Li, Kang and El Shiekh (1988), requires four distinct Cartesian motions of the yarns in the fabric cross-sectional plane in each machine cycle. Following G. W. Du (private communication, 1990), the 4-step braiding process is depicted in Fig. 7.4 for a 1×1 set-up in which the yarn carriers are arranged in a rectangular plane with eight columns ($m = 8$) and four layers ($n = 4$). Here, the yarn carriers are indicated by the circles, and can move along the y and z direction tracks. The process is termed 1×1 if the distance traveled by a carrier in each machine step is equal to the inter-yarn spacing in the y or z direction. Other braiding patterns (i.e. 1×2, etc.) are feasible, which require machine set-ups different from that of Fig. 7.4. It is noted that the carriers occupy alternating positions on the perimeter of the set-up. The total number of carriers in the $m \times n$ rectangular slab for the 1×1 braiding pattern is (Li, Kang and El Shiekh 1988):

$$N = mn + m + n = (m + 1)(n + 1) - 1 \tag{7.1}$$

Thus, for the 8×4 array, there are 44 carriers.

Consider the starting carrier positions as shown in Fig. 7.4(a). In step-1 of the machine cycle, all the rows of carriers move in the y direction; adjacent rows move in opposite directions as indicated by the arrows. In step-2 of the machine cycle (Fig. 7.4b), all the columns of carriers move vertically; adjacent columns move in opposite directions as indicated by the arrows. Note that in step-1 and step-2 movements, the carriers on the perimeter of the set-up remain stationary. The displacement of an individual carrier can be identified (for example, carriers marked A and B in Fig. 7.4a). Step 3 (Fig. 7.4c) is similar to step-1 except that the directions of movement of the same row are opposite to each other. The same comparison can be made between step-2 and step-4 (Fig. 7.4d). These four steps comprise a machine cycle, because at the end of the cycle (Fig. 7.4e) the carrier arrangement is the same as that at the beginning of the machine cycle, although the individual carriers have changed their locations.

It is interesting to note that the 44 carriers in the slab of Fig. 7.5(a) can be divided into four groups. These are denoted as groups

Fig. 7.4. Yarn carrier configurations and movements in a 4-step braiding set-up. (After G. W. Du, private communication, 1990.)

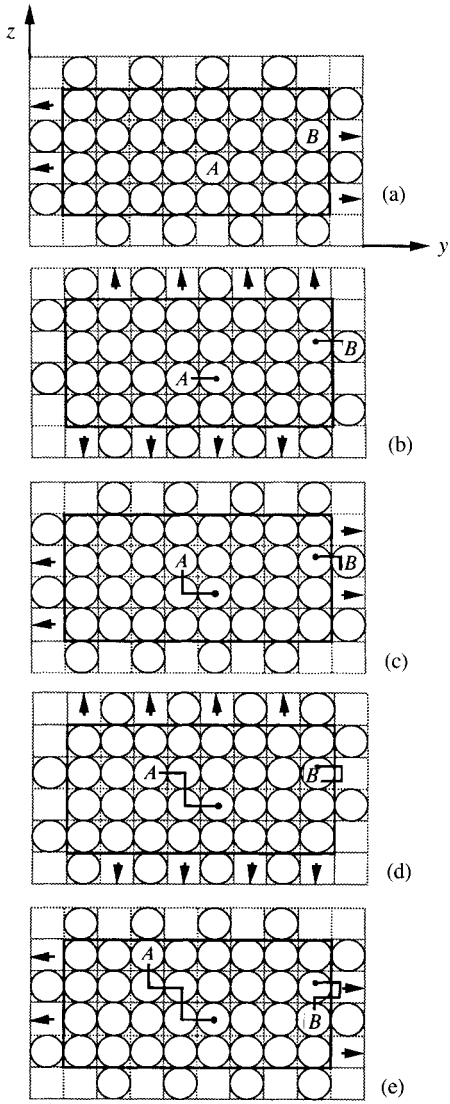

Fig. 7.5. The four yarn carrier groups in an 8×4 slab. Each group defines a unique yarn path. (a) Yarn carrier location; (b) carrier path for group 1; (c) carrier path for group 2; (d) carrier path for group 3; and (e) carrier path for group 4. (After G. W. Du, private communication, 1990.)

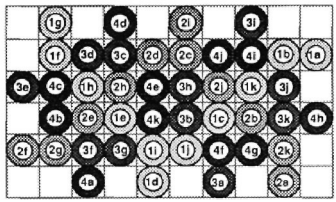

(a)

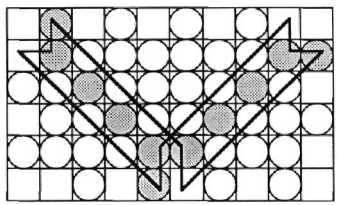

(b)

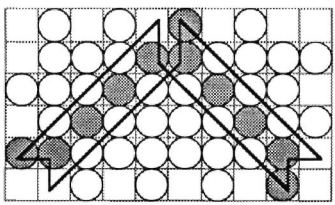

(c)

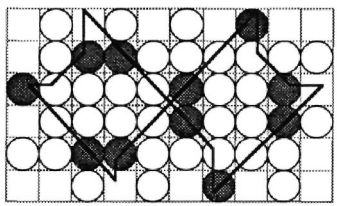

(d)

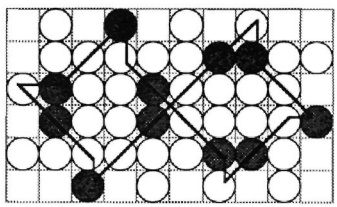

(e)

1, 2, 3 and 4. Within each group the carriers are labeled in alphabetical order from a to k. The characteristic of each group is that all the carriers within the group share the same path of motion. For example, carrier $1a$ in group 1, moves along the path of $1a \rightarrow 1b \rightarrow 1c \rightarrow 1d \rightarrow 1e \rightarrow 1f \rightarrow 1g \rightarrow 1h \rightarrow 1i \rightarrow 1j \rightarrow 1k \rightarrow 1a$ (Fig. 7.5b). All the other carriers in this group follow the same path. The paths of groups 2, 3 and 4 are indicated in Figs. 7.5(c), (d) and (e), respectively. The path for group 1 carriers in Fig. 7.5(b) is not marked directly on the carriers to avoid overlapping and confusion; the same is true for Fig. 7.5(c). The movement of a carrier, for instance, from position $1a$ to $1b$, or $1b$ to $1c$, etc. requires one machine cycle which comprises the steps as shown in Fig. 7.4. The complete cycle of movement of a carrier, i.e. $1a \rightarrow 1b \rightarrow \cdots \rightarrow 1a$ (returning to the original position) is termed a *repeat*.

Li, Kang and El Shiekh (1988) have shown that the number of yarn groups in an $m \times n$ slab is given by

$$G = mn/\mathrm{LCM}(m, n) \tag{7.2}$$

where $\mathrm{LCM}(m, n)$ denotes the least common multiple of m and n. Furthermore, each group has the same number of carriers, which is N/G. The number of machine cycles required for all the carriers to return to their original positions is thus also equal to N/G. It should be noted that the above discussions are valid only for the 1×1 braiding pattern.

7.2.1.3. *Solid braiding*

The term *solid braiding* is used here to describe the category of three-dimensional preforms produced by the continuous intertwining of yarns in the maypole fashion. Figure 7.6(a) shows the horn-gear set-up for square braiding. The longitudinal and cross-sectional views of some square braids are given in Fig. 7.6(b). Solid braids with circular cross-sections are also available. However, it is not feasible to produce three-dimensional preforms with complex shapes using solid braiding.

7.2.2 *Weaving*

Advances in textile manufacturing technology are rapidly expanding the number, type and complexity of preforms which offer reinforcements in the through-the-thickness direction. The traditional weaving technique for producing two-dimensional fabrics has been modified to achieve a much higher degree of integration in fiber geometry in the thickness direction. Angle-interlock weaving

and orthogonal weaving are the two distinct techniques by which the fibers are incorporated at an angle and parallel to the thickness direction, respectively.

7.2.2.1 *Angle-interlock multi-layer weaving*

Angle-interlock multi-layer woven fabrics for thick section composite applications can be produced on either a dobby loom or a Jacquard loom. The cam-system is limited to fabricating double- or triple-layer cloth. Yarns or fibers in angle-interlock multi-layer wovens are interlaced in a manner similar to two-dimensional woven structures, except that warp fibers may penetrate more than

Fig. 7.6. (a) Horngear set-up for square braiding. (After Ko 1989a.) (b) Examples of square braids. (After Steeger 1989.)

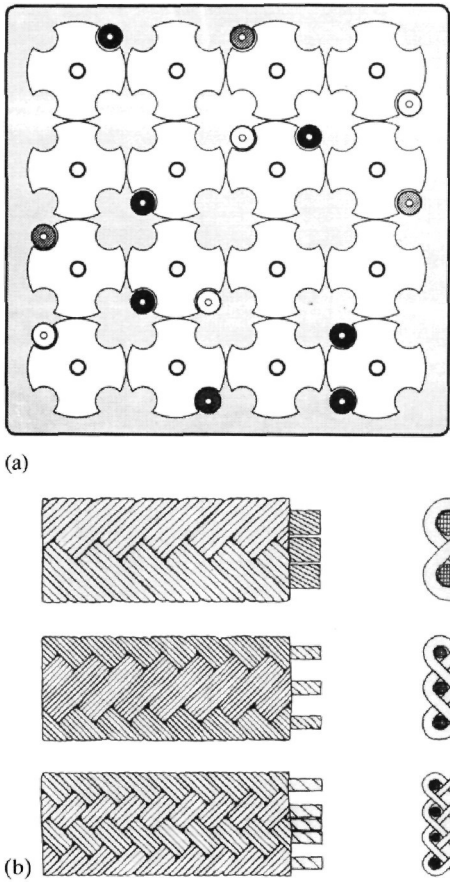

one layer of weft yarns. The warp direction again coincides with the machine direction, just as in two-dimensional wovens, whereas the filling yarn insertion takes place in the transverse direction. Many other preform configurations are possible, such as those with laid-in non-crimp yarns (to reduce Poisson's effect), or a combination of different fiber materials within the same preform (Whitney and Chou 1988, 1989).

Many variations in the basic geometry of angle-interlock preforms are feasible, depending on the number of layers interlaced, the pattern of repeat, and the presence of laid-in yarns. Whitney (1988) has discussed the fiber architectures in which all warp yarns interlace the same number of weft yarns. In order to demonstrate the geometric variability of angle-interlock fabrics, a highly idealized example is given in the following. Discussions are based on the fabric structure of the 1×1 pattern, i.e. the warp yarn orientation can be represented by one inter-yarn spacing in the horizontal direction and one inter-yarn spacing in the vertical direction, as shown in Fig. 7.7.

Following Byun, Leach, Stroud and Chou (1990a), the key geometric parameters for identifying the preform microstructure include the number of weft yarns in the thickness direction (n_f), as

Fig. 7.7. Three-dimensional angle-interlock woven preforms as identified by $[n_f, n_{ft}]$: (a) [5, 2], (b) [5, 4], and (c) [6, 6]. (After Byun *et al.* 1990.)

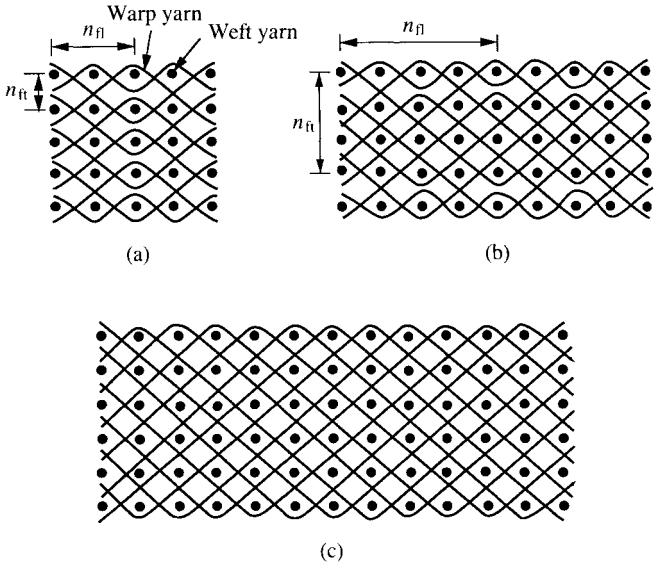

well as the number of weft yarns interlocked by a warp yarn in the thickness direction (n_{ft}) and in the length direction (n_{fl}). Parametric relations are obtained based on the preform structures which have the following restrictions: (1) The fabric structure is symmetric in the thickness direction with respect to the mid-plane. (2) The weft yarns have the same degree of interlocking by warp yarns. (3) The number of weft yarns in the thickness direction is the same along the warp direction. Employing the notation of $[n_f, n_{ft}]$, the woven preforms of Figs. 7.7(a), (b) and (c) can be identified as [5, 2], [5, 4] and [6, 6].

The following relationship needs to be satisfied to ensure the interlocking of weft yarns by warp yarns for the 1×1 pattern:

$$n_{ft} = n_{fl} \tag{7.3}$$

With the above condition, a maximum number of warp yarns can be achieved in the preform. For a $[n_f, n_{ft}]$ weave, the total number of warp yarns (n_w) is $2n_f$. However, not every warp yarn interlocks with n_{ft} weft yarns. This can be seen from Figs. 7.7(a) and (b) where the warp yarns at the top and bottom faces only interlace with the weft yarns in the surface layers. The degree of reinforcement in the thickness direction is related to the number of warp yarns (n_{wi}) that interlock with the n_{ft} weft yarns. When $n_f = n_{ft}$, all the warp yarns interlock with all n_{ft} weft yarns, i.e. $n_{wi} = 2n_{ft}$. When $n_f \neq n_{ft}$, n_{wi} is given as follows:

$$n_{wi} = 2kn_{ft} \qquad \text{for } k < n_f/n_{ft} < k+1 \tag{7.4}$$

$$n_{wi} = (2k-1)n_{ft} \qquad \text{for } n_f/n_{ft} = k \qquad (k \geq 2) \tag{7.5}$$

where k is an integer. For the fabrics of Figs. 7.7(a), (b) and (c), the n_{wi} values are, respectively, 8, 8 and 12.

Thus, the number of warp yarns (n_{wn}) which do not interlace n_{ft} weft yarns is

$$n_{wn} = 2n_f - n_{wi} \tag{7.6}$$

In Figs. 7.7(a) and (b), $n_{wn} = 2$ and in these cases each warp yarn at the surface only interlace with one layer of weft yarns. However, the n_{wn} warp yarns can also interlace with the multi-layer of weft yarns. Consider a fabric preform with the [5, 3] weave pattern and $n_{wn} = 4$. Figures 7.8(a) and (b) show the two possible configurations of the warp yarns near the free surfaces.

When the condition of Eq. (7.3) is not satisfied, the resulting fabric is not highly integrated and there are non-interlaced yarns. In

the following, the case of three-dimensional weaves with non-interlaced weft yarns is discussed. An additional geometric parameter, n_{ws}, is identified; it denotes the number of weft rows shifted by adjacent warp planes. Using the notation of $[n_f, n_{ft}, n_{ws}]$, the fabrics of Figs. 7.9(a), (b) and (c) can be identified as $[6, 2, 1]$, $[5, 3, 0]$ and $[5, 3, 1]$, respectively.

Finally, the total number of warp yarns can be obtained as

$$\begin{aligned} n_w &= n_f + 1, & n_f &\geq 3 & \text{for } n_{ft} &= 2 \\ n_w &= n_f + n_{ws} - 1, & n_f &= 2n_{ft} + 1 & \text{for } n_{ft} &\geq 3 \end{aligned} \tag{7.7}$$

Thus, the number of warp yarns interlaced through the n_{ft} weft yarns is

$$n_{wi} = n_w - 2n_{ws} \tag{7.8}$$

It should be noted that the parametric relations for a three-dimensional weave in which every weft yarn is interlocked with warp yarns can also be obtained in the case that Eq. (7.3) is not satisfied.

Fig. 7.8. Two variations of the $[5, 3]$ weave with $n_{wn} = 4$. the two warp yarns near the surface interlace with (a) one weft yarn layer or (b) two weft yarn layers. (After Byun *et al.* 1990.)

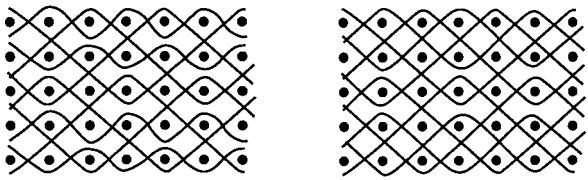

Fig. 7.9. Three-dimensional angle-interlock woven preforms as identified by $[n_f, n_{ft}, n_{ws}]$: (a) $[6, 1, 1]$, (b) $[5, 3, 0]$, and (c) $[5, 3, 1]$. (After Byun *et al.* 1990.)

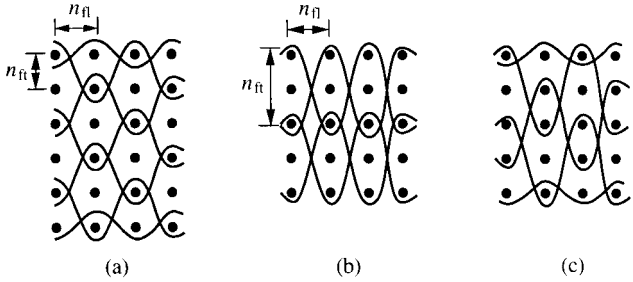

7.2.2.2 *Orthogonal weaving*

Figure 7.10 shows an orthogonal woven fabric where the yarns are placed in three mutually orthogonal directions. Because of the nature of fiber placement, matrix rich regions are created in composites reinforced with orthogonal woven preforms. Since the thickness direction yarns are incorporated into the preform in the weaving process, they do not cause damage to the in-plane fibers. This is different from the case of stitching bonding of two-dimensional fabrics. Orthogonal woven fabrics can be fabricated by maintaining one stationary axis either by predeposition of the yarn system or a space rod which is subsequently retracted and replaced by axial yarns. The two sets of yarns in the plane perpendicular to the axial yarns are then inserted in an alternating manner (Ko 1989a). Both Cartesian and cylindrical woven fabrics are available.

7.2.3 *Stitching*

The process of stitching for making three-dimensional preforms is relatively simple. The basic needs include a sewing machine, needle and stitching thread. The processing variables are stitch density (stitch/unit length), the size of the stitch thread, and types of stitch. Both lock stitch and chain stitch are available (Fig. 7.11). A lock stitch becomes unbalanced if the tension in either the bobbin thread or the needle thread is higher than that in the other thread. The necessary clearance between the feed and dog as well as the length of the needle stroke in the case of lock stitching, for instance, are

Fig. 7.10. An orthogonal woven fabric. (After Chou, McCullough and Pipes 1986.)

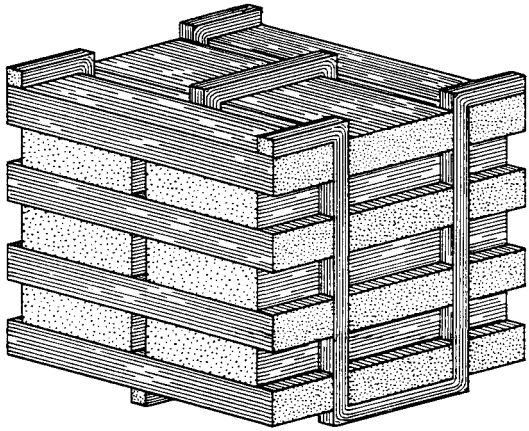

Fig. 7.11. (a) Lock stitch and (b) chain stitch seams. (After Ogo 1987.)

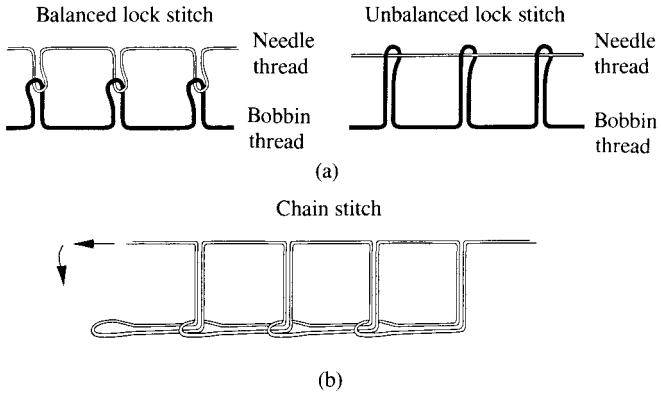

Fig. 7.12. Schematic of the lock stitch process. (After Ogo 1987.)

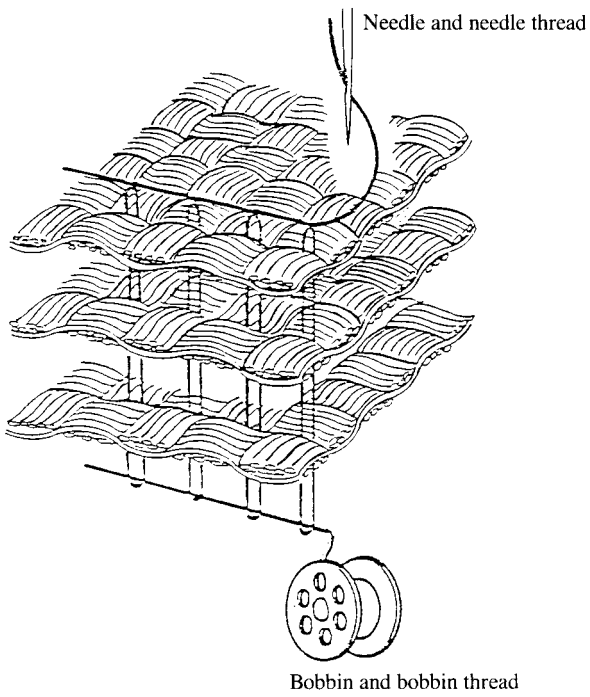

determined by the thickness of the two-dimensional preform to be stitch-bonded. Figure 7.12 shows the schematic of a lock-stitching process for bonding fabric layers. The needle thread needs to be abrasion resistant and can be bent to small curvature in the needle hole.

7.2.4 *Knitting*

Three-dimensional knitted fabrics can be produced by either a weft knitting or warp knitting process. For additional strengthening in the 0° and 90° directions, laid-in yarns can be placed inside the knitting loops. Figure 7.13 shows a weft knit fabric with laid-in weft and warp yarns.

The most promising knitted preform which provides a high degree of structural integration in the thickness direction is perhaps the multi-axial warp knit. It consists of warp (0°), weft (90°) and bias ($\pm\theta$) yarns held together by a chain of tricot stitch through the thickness of the assembly (Fig. 7.14). Different kinds of multi-axial warp knits have been developed. The main attraction of the knitted construction is that it possesses the advantage of unidirectional laminates while also providing enhanced stiffness and strength in the thickness direction (Ko, Pastore, Yang and Chou 1986).

7.3 Processing windows for 2-step braids

The purpose of the following discussions is to demonstrate that knowledge of the microgeometry and structure of textile preforms provides the basis for understanding flexibility in processing. The work of Du, Popper and Chou (1991) in 2-step braiding is recapitulated as an example of such an approach. The

Fig. 7.13. Weft knit with laid-in weft and warp yarns. (After Ko 1989a.)

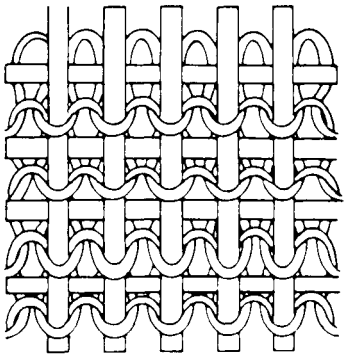

key inputs of the analysis are (1) the size, type and shape of braiders and axial yarns, (2) the braid pattern (size of axial yarn array), and (3) the advance rate during braiding. The key outputs are braid dimensions, fiber orientation, inter-yarn void content, fiber volume fraction, and geometric limits imposed by yarns jamming against each other. The modeling work is for preforms of rectangular cross-section. However, the methodology regarding yarn cross-sections, unit cells, and yarn jamming can be used to analyze more complex shapes, as well as other types of three-dimensional fabrics.

The major assumptions are: (1) Multi-filament yarns are used for both braiders and axial yarns. These yarns are composed of a large number of fibers, and their cross-sections can be readily deformed to prismatic shapes. (2) Fiber cross-section is round. (3) Fibers are parallel along the yarn length, i.e. zero twist. (4) Yarn tension is high enough to ensure a straight yarn path, except for the braider yarns, which are bent around the braid surface. (5) Filaments are inextensible.

7.3.1 *Packing of fibers and yarn cross-sections*

The fiber volume fraction of a three-dimensional preform depends on the level that fibers pack against one another in a yarn and the level to which yarns pack against one another in the structure. Two methods for estimating inter-fiber packing are described in this section. Section 7.3.3 discusses yarn packing in preforms.

The geometry of inter-fiber packing in yarns has been studied primarily for textile applications (see Hearle, Grosberg and Backer

Fig. 7.14. Mult-axial warp knit fabric. (After Chou, McCullough and Pipes 1986.)

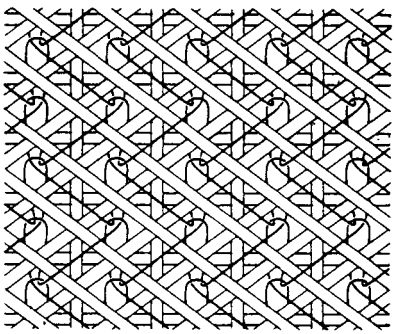

1969). Two basic idealized packing forms can be identified: open packing (Fig. 7.15a) and close packing (Fig. 7.15b), in which the fibers are arranged in concentric and hexagonal patterns, respectively.

In open-packed yarns the packing fraction, defined as the fiber-to-yarn area ratio, has been computed as a function of the number of fibers. If the outer ring is completely filled and the fibers are circular, the yarn packing fraction is

$$\kappa_o = \frac{3N_r(N_r - 1) + 1}{(2N_r - 1)^2} \tag{7.9}$$

where N_r is the number of rings, and its relationship to the number of fibers, N_f, is given by

$$N_r = \tfrac{1}{2} + \sqrt{(\tfrac{1}{4} + \tfrac{1}{3}(N_f - 1))} \tag{7.10}$$

For a large number of fibers, κ_o approaches 0.75.

In close-packed yarns, for any number of circular fibers if the outer layer is completely filled, the yarn packing fraction equals the

Fig. 7.15. Fiber packing in yarns. (a) Open packing in a circular yarn. (b) Close packing in a hexagonal yarn. (c) Open packing in a diamond-shaped yarn. (d) Close packing in a diamond-shaped yarn. (After Du, Popper and Chou 1991.)

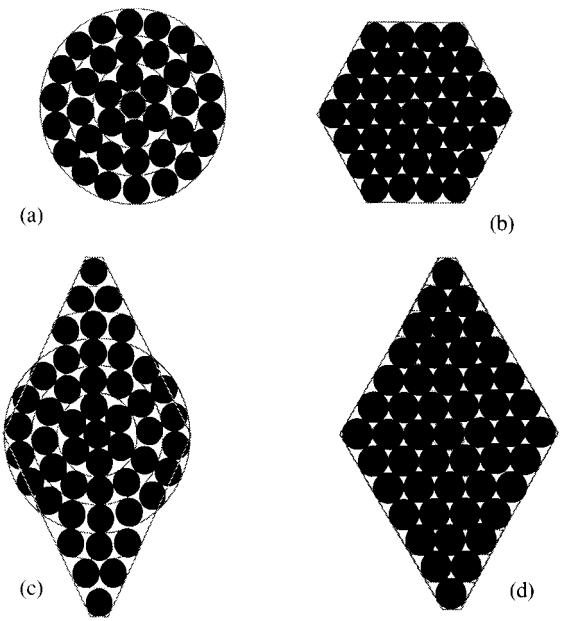

area ratio of a circle to the hexagon in which the circle is inscribed:

$$\kappa_c = \frac{\pi}{2\sqrt{3}} = 0.91 \tag{7.11}$$

The yarn packing fractions predicted by the two models assume circular and hexagonal yarn cross-sections. However, as shown in Figs. 7.15(c) and (d), they apply equally well to other shapes if the number of fibers is sufficiently large. Factors that affect both the packing of fibers in a yarn and the packing of yarns in a preform include yarn tension, inter-yarn contact, yarn twist, fiber cross-section, fiber straightness, manufacturing method, and preform geometry.

In addition to the level of yarn packing fraction, the yarn cross-sectional shape plays a significant role in determining how many fibers can be packed into a fabric. In the textile literature, the yarns are often assumed to have a circular cross-section (see Peirce 1937; Brunnschweiler 1954). However, it has been shown that the cross-section of even highly twisted yarns deviates significantly from a circular shape and the yarn cross-section varies considerably for different types of preforms. Many attempts have been made to develop more realistic geometric models for yarns in fabrics by assuming elliptical and race-track cross-sections (Hearle, Grosberg and Backer 1969).

Fig. 7.16. Cross-sections of axial yarns in a rectangular braided preform before consolidation. (After Du, Popper and Chou 1991.)

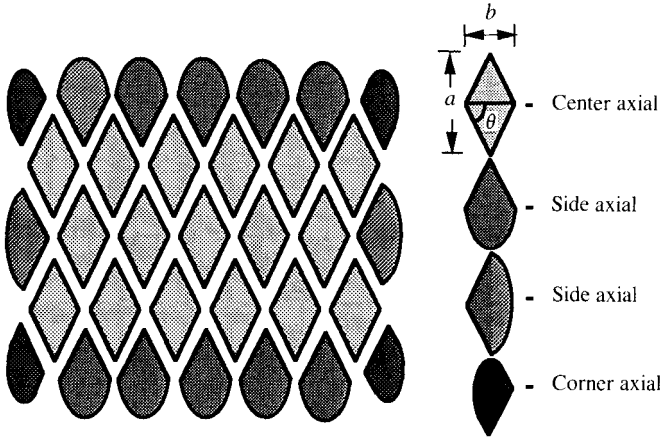

In the following, a model for the yarn cross-section in 2-step braids is developed. It is observed from composite specimens that the yarns in the preform have cross-sections as shown in Fig. 7.16. After matrix addition and consolidation in a mold, the fabric is observed to be flattened, as shown in Fig. 7.17. The axial yarns have different cross-sections depending on their locations in the preform. Central yarns, which form the bulk of the structure, are diamond-shaped. Axial yarns on the side and corners of the preform are pentagonal. Braiding yarns, which occupy the space in between the axial yarns, are rectangular.

The aspect ratio of axial yarns, f_a, is related to the inclination angle of the braiders (Figs. 7.16 and 7.18) and is given by

$$f_a = \frac{a}{b} = \tan\theta \tag{7.12}$$

where f_a is influenced by braider yarn tension or external lateral compression applied at the forming point during the process. It can also be changed by compacting the entire braided preform during matrix consolidation. These aspect ratios affect the shape of the final braid as well as the braider yarn orientation angle (α) and fiber volume fraction (V_f). With unit axial aspect ratio ($\theta = \pi/4$), the cross-section of the center axial yarns becomes square. In this special case, the fiber volume fraction is at a maximum.

The axial yarn dimensions can be calculated from the cross-section of the consolidated braid in Fig. 7.17. These relations are

Fig. 7.17. Cross-sections of axial yarns in a rectangular braided composite. (After Du, Popper and Chou 1991.)

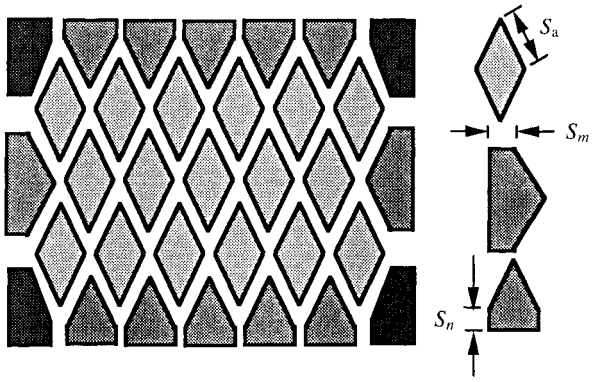

given in terms of yarn area and inclination angle. The yarn area is in turn evaluated from its linear density and the fiber packing fraction and fiber density:

$$S_a = \sqrt{\left(\frac{\lambda_a}{\rho_a \kappa_a \sin(2\theta)}\right)}$$

$$S_m = \frac{0.5\lambda_a}{2S_a \rho_a \kappa_a \sin\theta} \tag{7.13}$$

$$S_n = \frac{0.5\lambda_a}{2S_a \rho_a \kappa_a \cos\theta}$$

The parameters λ_a and ρ_a are the linear density and the fiber density of axial yarns, respectively. The packing fraction, κ_a, is assumed to be constant for all axial yarns.

Fig. 7.18. Path of one braiding yarn in the fabric: (a) braid pattern ; (b) top view; and (c) front view. (After Du, Popper and Chou 1991.)

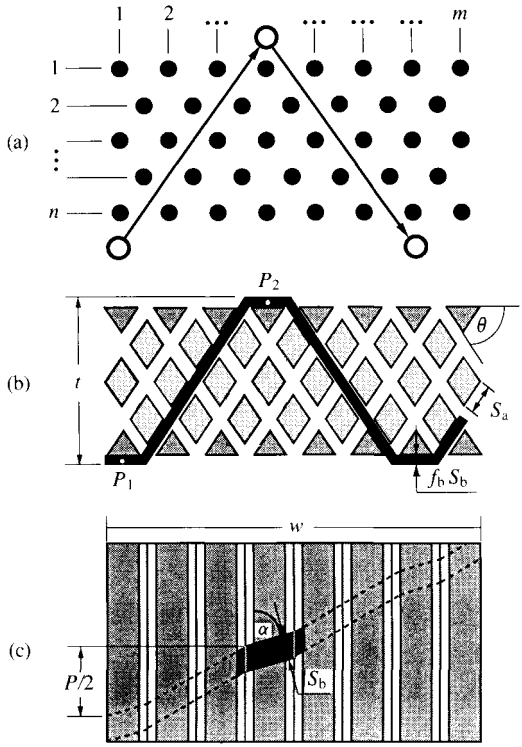

For, only one braider yarn is shown in Fig. 7.18 for two steps of the braiding process. These yarns are assumed to be rectangular with aspect ratio f_b. The aspect ratio is usually much less than unity because of compression by the axial yarns. The dimension of a braider yarn can also be calculated from its packing fraction (κ_b), yarn linear density (λ_b), and fiber density (ρ_b):

$$S_b = \sqrt{\left(\frac{\lambda_b}{\rho_b \kappa_b f_b}\right)} \tag{7.14}$$

7.3.2 *Unit cell of the preform*

In order to understand the microscopic arrangements of yarns, it is necessary to identify the 'unit cell' of the fabric preform. By definition, a unit cell constitutes the smallest repeating entity in the structure. The complexity of three-dimensional preform structures often makes the identification of unit cells a difficult task.

The unit cell of the 2-step braid is composed of four sub-cells, labelled A, B, C and D in Fig. 7.19. The repeat of these four sub-cells will generate the whole braided structure. Because of geometric similarity, any one of these four can be utilized to derive the basic structural characteristics. The length of the unit cell in Fig. 7.19 is the length of braid formed in one machine step. This length is actually half of the fabric pitch length (P), as shown in Figs. 7.18–7.20. Five layers are shown in Fig. 7.19. The number of columns has been assumed to be very large so that the rather complicated edge configuration of the preform can be avoided. Figure 7.20 shows the difference between finite and infinite columns and their effects on braider paths. Figure 7.20(a) shows the yarn path on the surface of a specimen seven columns wide. Note that the trace of the braider yarns lies on an inclined line. In an infinitely wide specimen (Fig. 7.20b) the trace of the braider yarns is perpendicular to the braiding direction.

The width and thickness of the braided preform can be computed from Figs 7.17 and 7.18 in terms of m (number of axial columns) and n (number of axial layers) as well as yarn geometric and material parameters:

$$w = (m-1)\left(2S_a \cos\theta + \frac{f_b S_b}{\sin\theta}\right) + 2(S_m + f_b S_b) \tag{7.15}$$

$$t = (n-1)\left(S_a \sin\theta + \frac{f_b S_b}{2\cos\theta}\right) + 2(S_n + f_b S_b) \tag{7.16}$$

From Eqs. (7.15) and (7.16), the aspect ratio of the braided preform can be obtained as

$$f = \frac{t}{w} \tag{7.17}$$

The braider yarn orientation can be determined by computing the *projected* length (i.e. segment P_1P_2 in Fig. 7.18b) of one braider over one half of the pitch length. Note that the angle between a braider and the axial yarns (α) appears to vary on the front view in Fig. 7.18(c). This apparent variation occurs because a segment of a braider yarn in the interior of the preform has a different projected angle compared to a segment on the preform surface. The projected

Fig. 7.19. Unit cell model of a 2-step braided preform showing four sub-cells. Each sub-cell includes a braider yarn and a number of axial yarns. (After Du, Popper and Chou 1991.)

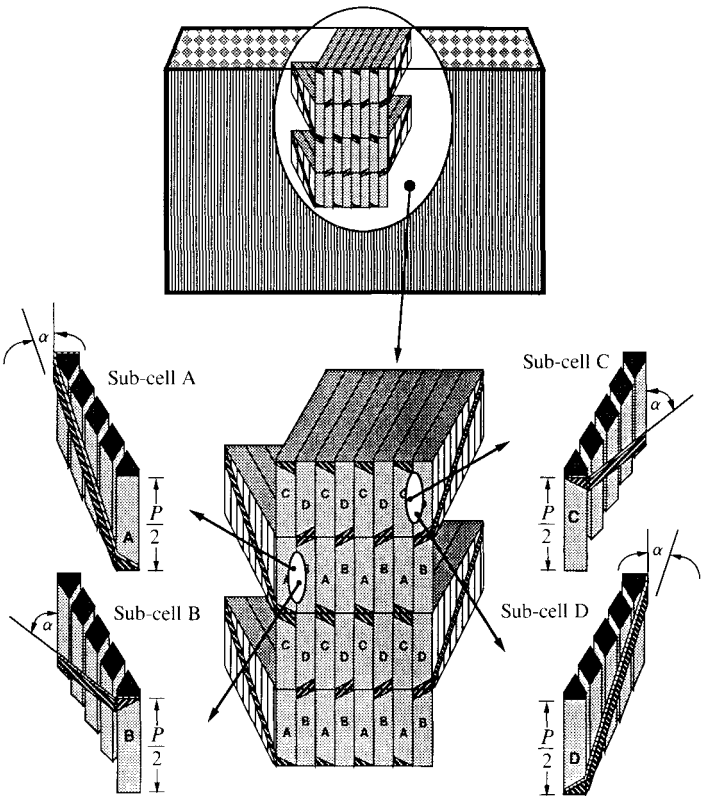

length L_p of the segment P_1P_2 in the axial direction is

$$L_p = t \csc\theta + 2S_n(1 - \csc\theta) + 2S_a \cos\theta \tag{7.18}$$

The braider yarn angle is then given by

$$\alpha = \tan^{-1}\left(\frac{2L_p}{P}\right) \tag{7.19}$$

The total length of one braider yarn in a unit cell is

$$L_b = \frac{L_p}{\sin\alpha} = \frac{P}{2\cos\alpha} \tag{7.20}$$

Then the volume of the braider yarn (v_b) and the volume of axial yarns (v_a) in a unit cell and the total volume of a unit cell (v_t) can be determined:

$$v_b = L_b f_b S_b^2 \tag{7.21}$$

$$v_a = \frac{P}{2} S_a[(n-1)S_a \sin(2\theta) + 4S_n \cos\theta] \tag{7.22}$$

$$v_t = v_a + \frac{P}{2} f_b S_b[(n-1)S_a + L_p] \tag{7.23}$$

The fiber volume fraction V_f (total fiber volume/unit cell volume), the braider fiber volume fraction V_b (braider fiber volume/unit cell volume), and the volume fraction of the void V_v (volume of

Fig. 7.20. Effect of fabric width on braid geometry: (a) finite-width preform; (b) infinite-width preform. (After Du, Popper and Chou 1991.)

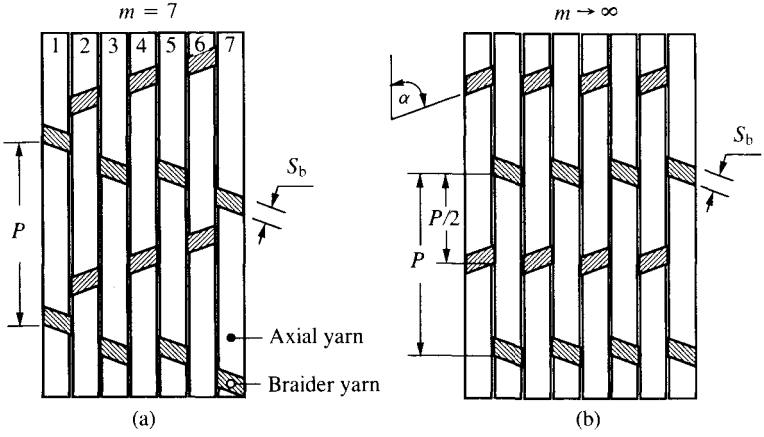

inter-yarn voids/unit cell volume), can then be obtained:

$$V_f = \frac{v_a K_a + v_b K_b}{v_t} \tag{7.24}$$

$$V_b = \frac{v_b K_b}{v_t} \tag{7.25}$$

$$V_v = 1 - \frac{v_a + v_b}{v_t} \tag{7.26}$$

7.3.3 *Criterion for yarn jamming*

The allowable microstructural states of a fabric preform are limited by the condition at which the yarns jam against one another. Knowledge of yarn jamming is essential in identifying the processing windows of fabric preforms. Although jamming is discussed frequently in the textile literature, it is often neglected in the analysis of composites.

In 2-step braids, the braider angle becomes very small as the braider yarns become parallel to the axial yarns. However, as the pitch length is reduced, the braider angle increases, and a limiting state is reached in which the yarns jam against one another. If all other parameters remain constant, the pitch length cannot be reduced further. The state of jamming is illustrated in Fig. 7.21 where the yarn-to-yarn contact is shown. This rather complex

Fig. 7.21. Surface geometry of braid at jamming. (After Du, Popper and Chou 1991.)

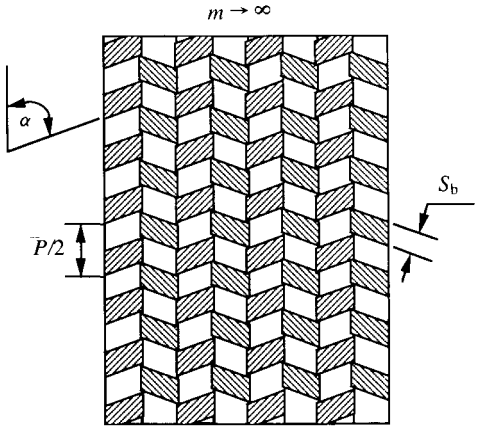

limiting state, however, can be described simply by

$$P_j = \frac{2S_b}{\sin \alpha} \tag{7.27}$$

where P_j denotes the pitch length at jamming. Equation (7.27) is applicable to specimens of finite width.

Due to the edge effect of finite-width structures, the orientation angle, α, of all braiders are not equal. In a braiding step, the braiders on the side surface of the preform will have shorter length than those in the interior. However, since all yarns advance at the same pitch length, the 'edge' braiders will lie at a somewhat lower angle than those passing through the center of the structure.

Du, Popper and Chou (1991) have conducted experiments to measure the geometric and material parameters of 2-step braids. A comparison of measured and predicted values of two samples are given in Table 7.1. Braid I is rectangular in cross-section, consisting of 12-column by five-layer axial yarns (Kevlar-49 with a linear

Table 7.1 *Material and geometric parameters of 2-step braided preforms. After Du, Popper and Chou* (1991)

	Braid I		Braid II	
Parameters	Measured	Computed	Measured	Computed
λ_a (g/m)	9.57		3.33	
λ_b (g/m)	2.39		0.25	
m	12		7	
n	5		5	
P (mm)	17.8		4.98	
f_a	0.78		1.32	
f_b	0.12		0.05	
κ_a	0.70		0.78	
κ_b	0.70		0.78	
t (mm)	9.0	8.9	7.0	7.3
w (mm)	63.0	62.9	15.0	14.6
α (°)	65.0	65.9	75.0	76.7
V_f (%)	56.0	56.8	73.0	73.6

Braid I: bare fiber preform.
Braid II: infiltrated with matrix.

density of 9.57×10^{-3} kg/m) and 15 braider yarns (Kevlar-49 with a linear density of 2.39×10^{-3} kg/m). Braid II is also rectangular in cross-section, with seven-column by five-layer axial arrays and ten braiders. In Braid II, all axial yarns are made of Kevlar-29 with a linear density of 3.33×10^{-3} kg/m: Kevlar-49 is used for the braider yarns which are much finer than the axial yarns with a linear density of 2.53×10^{-4} kg/m. Braid II was impregnated with an epoxy by resin transfer molding.

Based upon the relations between process variables and fabric geometry, it has been shown that the range of allowable fabric structures is dictated by effects such as yarn jamming and fiber packing. Figure 7.22 demonstrates the processing window for 2-step braids when the braider yarn orientation angle and pitch length, total fiber volume fraction, and yarn linear densities are considered. The processing window is bounded by two limiting states: yarn jamming and zero braider angle. Preform constructions corresponding to the curved 'jamming' line are at their tightest possible state, and constructions corresponding to the $\alpha = 0$ curve have infinite pitch length. As the dimensionless pitch length P/S_a increases, the

Fig. 7.22. Fiber volume fraction vs. braider-to-axial linear density ratio. The allowable process window is shown ($\kappa_a = 0.8$, $\kappa_b = 0.8$, $\theta = 38°$, $f_b = 0.2$, $n = 5$). (After Du, Popper and Chou 1991.)

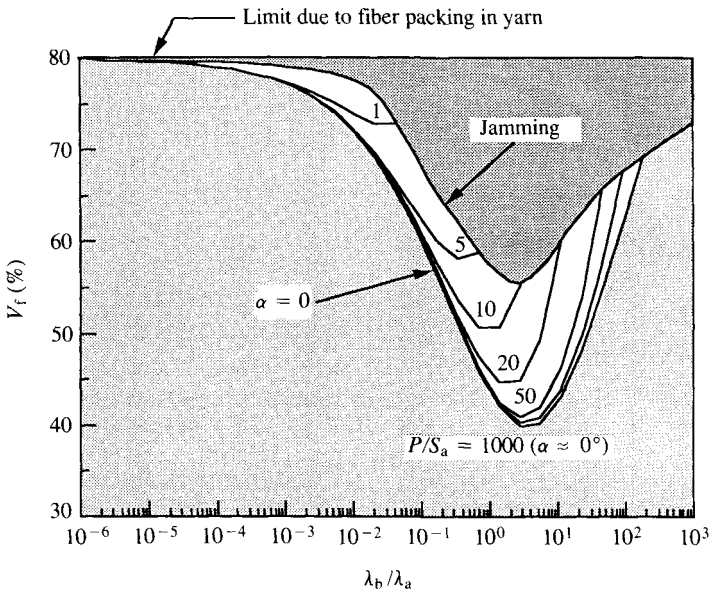

fiber volume fraction decreases. Increasing the ratio of braider-to-axial yarn linear density causes the maximum allowable fiber volume fraction to go through a minimum. At fixed levels of pitch length, an increase in λ_b/λ_a first reduces the fiber volume fraction because the inclusion of larger braider yarns creates more void space. However, at large λ_b/λ_a ratios, a higher fiber volume fraction is realized. At a ratio of about 200, the fabric reaches a limiting state in which the braider yarn angle approaches zero due to the infinite pitch length. The fiber packing in the yarns, taken as 0.8, limits the maximum fiber volume fraction in the fabric.

A 'microstructure map' of 2-step braids, which gives the relationship among fiber volume fraction, pitch length, braider yarn orientation angle and braider yarn volume fraction, is shown in Fig. 7.23. The minimum allowable fiber volume fraction increases with a reduction in braider yarn pitch length. For a fixed pitch length and above the minimum allowable fiber volume fraction, both V_f and α increase with an increase in braider fiber volume fraction. This map demonstrates that a wide range of orientation angle and fiber volume fraction can be achieved by varying the pitch length and the amount of braider yarns relative to the axials. Maps of microstructures provide guidance in designing preforms for a specific application.

Fig. 7.23. Property volume fraction (V_f) vs. fiber orientation angle (α) for various pitch length and volume fraction of braider yarns ($\kappa_a = 0.8$, $\kappa_b = 0.8$, $\theta = 38°$, $f_b = 0.2$, $n = 5$). (After Du, Popper and Chou 1991.)

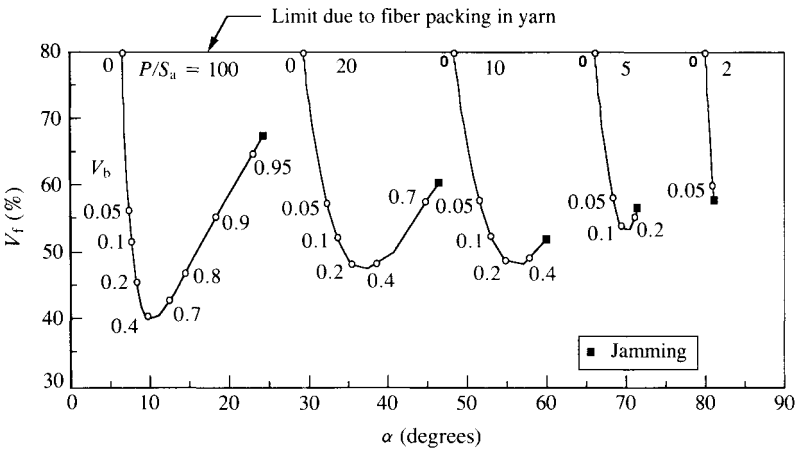

7.4 Yarn packing in 4-step braids

Knowledge of yarn packing in three-dimensional structures is essential for determining the unit cell configuration of a fiber preform as well as the condition for yarn jamming. In a 4-step braiding process, the braiding yarn carriers move in a two-dimensional grid with two sets of perpendicular tracks (Fig. 7.4). For the sake of simplicity, the following discussions are restricted to 4-step braids without laid-in yarns.

7.4.1 *Unit cell of the preform*

When the specimen cross-sectional area is large, the dominant unit cell configuration can be represented by a parallelepiped (Fig. 7.24) with the size of $P_a \times P_b \times P_c$. The braiding axis is assumed to coincide with the x axis. Obviously, for a 1×1 braid, $P_b = P_c$. A unit cell contains four yarns situated along the diagonals. It is understood that in Fig. 7.24 the yarns are idealized as geometric lines and, thus, they intersect at the center of the unit cell.

The details of the yarn arrangement in a 1×1 braid can be visualized by taking the 123′4′ cross-section of the unit cell. This is

Fig. 7.24. Unit cell of a 4-step braided preform. (After Yang, Ma and Chou 1986).

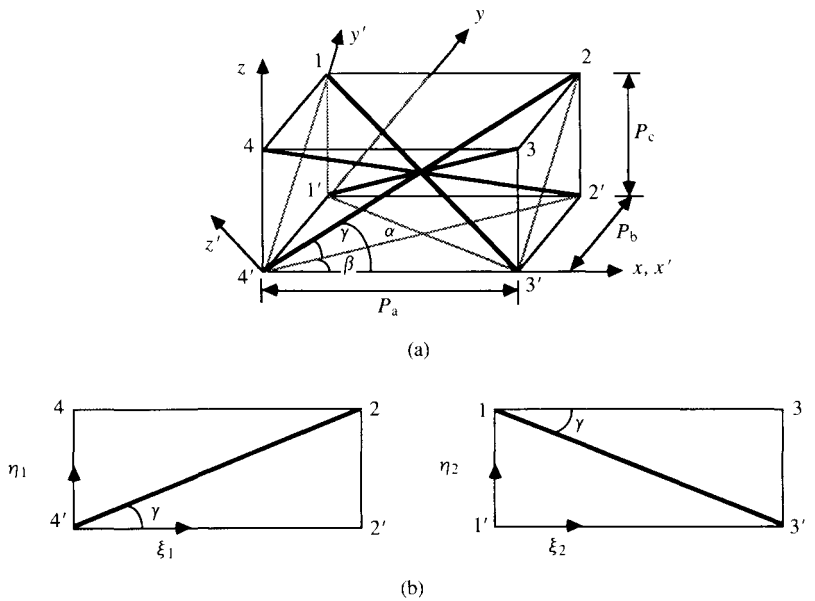

shown in Fig. 7.25. Referring to Fig. 7.24, the yarns along the diagonals 13′ and 4′2 are contained in the cross-section, and are at an angle α to the braiding axis. Yarns of type 4′2 are shown in Fig. 7.25 by the inclined sections. Yarns of types 1′3 and 2′4 show elliptical sections. Yarns of type 13′ are also parallel to the cross-section and they are blocked by the other three types of yarns in the cross-sectional view of Fig. 7.25.

It should be noted that Fig. 7.25 is valid for $\alpha < 58°$, which is the critical angle for yarn jamming (Section 7.4.2). The pitch length, P, which is the preform take-up length for one machine cycle (four steps), is defined in Fig. 7.25, along with the braider yarn orientation angle α.

7.4.2 *Criterion for yarn jamming*

The condition for yarn jamming in a 4-step braided preform can be understood from the yarn geometric arrangements. The following assumptions are made in the derivation of the yarn jamming criterion: (1) the braiding yarns are circular in cross-section, with diameter d, (2) the yarns are in a stable configuration, namely, each yarn in Fig. 7.24 is in contact with the other three, and (3) the braid is of the 1×1 type.

Fig. 7.25. Fiber configuration in the cross-section 4′3′21 of Fig. 7.24. (After G. W. Du, private communication, 1990.)

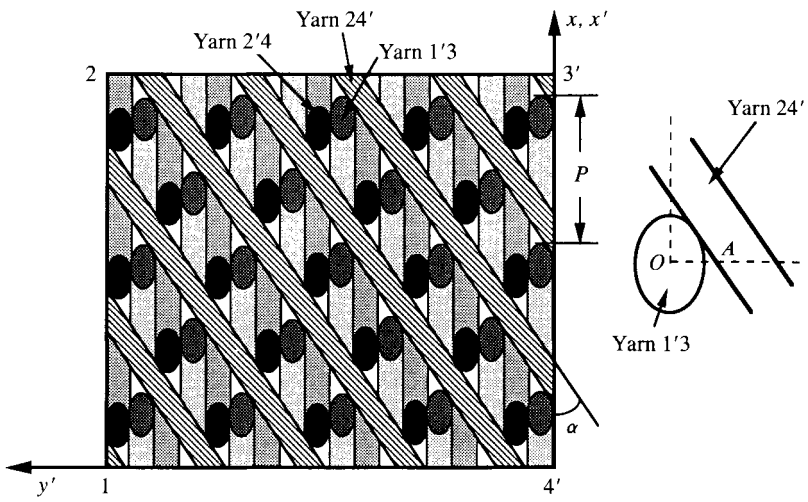

Figure 7.25 shows the yarn configuration of the cross-sectional plane 123′4′ before yarn jamming. The pitch length and fiber diameter are denoted by P and d, respectively. From the relation of tangency between an ellipsoid (yarn 1′3) and a line (yarn 24′), the distance OA can be obtained:

$$OA = \frac{d}{2}\sqrt{(1 + \sec^2 \alpha)} \tag{7.28}$$

Another geometric relation for this yarn configuration is

$$P \tan \alpha = 4d = d(1 + \sec \alpha + \sqrt{(1 + \sec^2 \alpha)}) \tag{7.29}$$

which yields the braider yarn angle and aspect pitch length (P/d):

$$\alpha = 41.4°; \qquad P/d = 4.54 \tag{7.30}$$

As compaction of preform continues, the yarn configuration finally reaches a limiting state where both the yarns 2′4 and 1′3 touch the yarn 24′. Figure 7.26 shows the yarn configuration at jamming. The geometric relation for this case is:

$$P \tan \alpha = 4d = d(\sec \alpha + \sqrt{(1 + \sec^2 \alpha)}) \tag{7.31}$$

Thus, the criteria for yarn jamming are

$$\alpha = 57.8°; \qquad P/d = 2.52 \tag{7.32}$$

and the conditions $\alpha > 57.8°$ and $P/d < 2.5$ are physically not feasible. It is interesting to note that jamming in 4-step braids occurs at a unique yarn orientation angle, which is independent of the yarn material and processing parameters.

Fig. 7.26. Yarn configuration at jamming (After G. W. Du, private communication, 1990.)

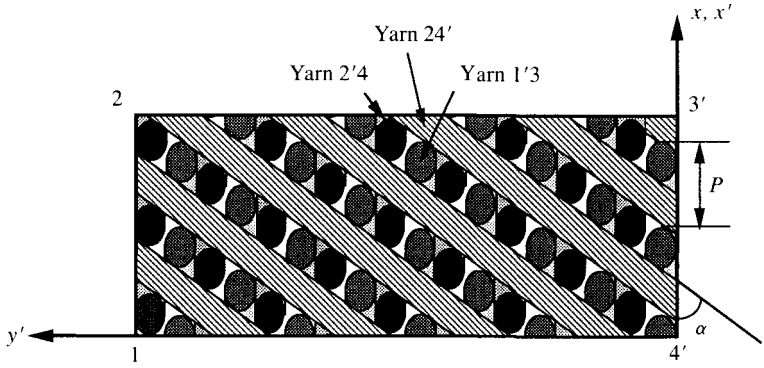

The consequence of such a characteristic of 4-step braiding is the absence of a processing window for providing the flexibility of manufacturing. However, such a window can be created by using two or more types of braiding yarns and inserting laid-in yarns, thus expanding the ranges of fiber geometric and material parameters.

7.5 Analysis of thermoelastic behavior of composites

The analysis of thermoelastic behavior of three-dimensional fabric composites can be made based upon the knowledge of the microstructure of the preforms. For the preforms reviewed in Section 7.2, their unit cell structures are sufficiently well established.

For braided composites, the unit cells of both 2-step and 4-step braids are well known, whereas the unit cells for solid braids depend on the specific preform designs. In the case of weaving, the unit cell of an angle-interlock woven may occupy the entire preform thickness. This is true for the preforms shown in Fig. 7.7 where there are no repeating units in the thickness direction. The unit cell structures of orthogonal wovens and stitch-bonded preforms are similar. Because the thickness direction yarns in both cases are normal to the free surfaces, they can be considered as limiting cases of the angle-interlock configuration.

The knitting yarns in a multi-axial wrap knit are severely curved. Because the knitting yarns usually have fine dimension and low stiffness, their contributions to the composite thermoelastic properties are perhaps negligible. When high stiffness knitting yarns are used, their contributions to the thickness direction properties need to be taken into account. Because of the low volume fraction of knitting yarns, relative to that of the in-plane fibers, it is not unreasonable to neglect the in-plane behavior of the knitting yarns in the composite.

Unlike the case of unidirectional laminates, the thermoelastic behavior of three-dimensional composites is complicated by the fiber configuration in the thickness direction. In the following, three different analytical approaches are outlined. Among them, the energy approach considers the elastic strain energies due to the interaction of yarns at an interlock. The fiber inclination model is based upon the lamination analogy, whereas the macro-cell approach utilizes stiffness tensor transformation and an averaging technique.

Besides these three modeling techniques, a micro-cell approach has been adopted by Whitney (1988) and Whitney and Chou (1989) for analyzing angle-interlock woven composites. This technique is also based upon the lamination analogy. In view of the large geometric variability of angle-interlock wovens, their elastic behavior perhaps can be more efficiently analyzed by the macro-cell approach.

7.5.1 *Elastic strain-energy approach*

An elastic strain-energy approach has been adopted by Ma, Yang and Chou (1986) to derive the elastic stiffness of three-dimensional textile structural composites. Although their analysis is for a 4-step braided composite, the methodology has general applicability.

In the general case, the unit cell structure of Fig. 7.24 can be considered as composed of three sets of mutually orthogonal yarns as well as yarns assuming the diagonal positions. The unit cell is centered on an 'interlock' of these yarns. The analytical model then then focuses on the interaction of the yarns at the center of the unit cell.

The following assumptions are made in the analysis: (1) The baseline and diagonal yarns are regarded as 'composite rods' after being impregnated with matrix materials. The stiffness and strength of the composite are mainly derived from the three-dimensional composite rod structure. (2) The composite rods are homogeneous and linearly elastic, and have uniform circular cross-sections that do not flatten under external loading. (3) The composite rods possess tensile, compressive, and bending rigidities. (4) A jamming force exists at the region of contact between two interlocking composite rods. The rods can be treated as either compressible or incompressible under the action of jamming forces.

Because of the complexity of the yarn configurations at their interlocking positions, the model does not simulate each individual 'lock' separately. The interactions among the yarns are dealt with in approximate fashion by projecting the yarn positions onto a set of mutually orthogonal planes. Within each two-dimensional projection, the interactions between two yarns are taken into account.

Consider, for instance, the interaction of two baseline composite rods (Fig. 7.27). Three types of elastic strain energies in the composite rods are taken into account. These include the strain energies due to bending, extension and compression over the region of fiber contact. Based upon the knowledge of the elastic strain energy of the baseline and diagonal composite rods, the elastic

properties of the composite can be obtained through the application of an energy principle.

7.5.2 *Fiber inclination model*

The fiber inclination model developed by Yang, Ma and Chou (1986) can be understood also by considering the yarn arrangements in a 4-step braided preform. Consider again the unit cell structure based upon the yarns oriented along the four body diagonals in a 4-step braided fabric (Fig. 7.24). The three-dimensional composite can thus be regarded as an assemblage of unit cells as shown in Fig. 7.28(a), where the emphasis is placed on the yarn orientation rather than the interaction among yarns. Here only one set of diagonal yarns in the composite is shown for clarity. The zig-zagging yarn segments are not confined to one layer only. Each yarn in the composite extends through the whole length of the material and changes its orientation at the interlocks. Furthermore, straight laid-in yarns along the edges of the unit cell can be added in the present formulation.

The methodology for the analysis of the fiber inclination model is based upon a modification of the classical laminated plate theory. The following geometrical characteristics are assumed by Yang, Ma and Chou (1986): (1) All the yarn segments parallel to a diagonal direction in the layer *ABCD* (Fig. 7.28a), for instance, are treated as forming an inclined lamina (Fig. 7.28b) after matrix impregnation. (2) Fibers within a lamina are considered to be straight and

Fig. 7.27. Yarn interaction at the point of interlock.

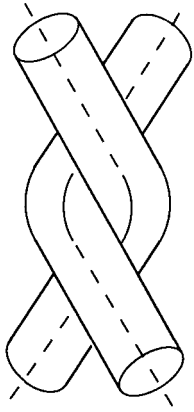

unidirectional. Fiber interlocking and bending due to the change of orientation from one diagonal direction to another at the corners of the unit cell are not taken into account. (3) A unit cell in Fig. 7.24(a) can be further considered as an assemblage of four inclined unidirectional laminae. The intersections among the four inclined laminae are ignored. Each unidirectional lamina is characterized by a unique fiber orientation and all the laminae have the same thickness. Furthermore, the fiber volume fraction of each lamina is assumed to be the same as that of the composite.

The laminate approximation of the unit cell structure is shown schematically in Fig. 7.29. The geometrical configuration and stacking sequence of the inclined laminae composed of yarns in four diagonal directions in the unit cell are given below. First, the $\xi_1 - \zeta_1 - \eta_1$ and $\xi_2 - \zeta_2 - \eta_2$ coordinate systems are assigned to

Fig. 7.28. (a) The idealized zig-zagging yarn arrangement in the braided preform. (b) Schematic view of the inclined laminae representing the diagonal yarns of the 'fiber inclination model'. (After Yang, Ma and Chou 1986.)

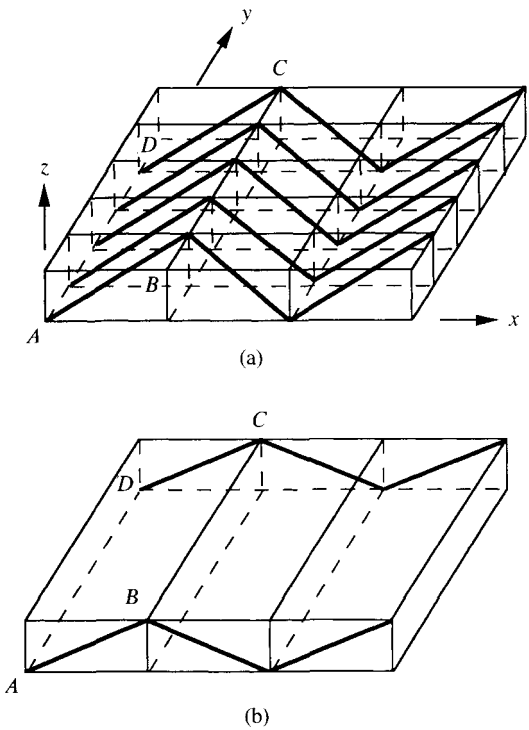

lamina 4′2′24 and lamina 1′3′31, respectively, as shown in Fig. 7.24(b). Referring to Figs. 7.24 and 7.29, the equations describing the height of each lower surface of laminae 1 and 3 and the height of each upper surface of laminae 2 and 4 measured from the base plane ($z = 0$) of the unit cell are:

$$\text{lamina 1 (yarn 4′2): } H_1(\xi_1) = \frac{P_c \xi_1}{L} \qquad (0 \le \xi_1 \le L) \tag{7.33}$$

$$\text{lamina 2 (yarn 1′3): } H_2(\xi_2) = \frac{P_c \xi_2}{L} \qquad (0 \le \xi_2 \le L) \tag{7.34}$$

$$\text{lamina 3 (yarn 42′): } H_3(\xi_1) = P_c\left(1 - \frac{\xi_1}{L}\right) \qquad (0 \le \xi_1 \le L) \tag{7.35}$$

$$\text{lamina 4 (yarn 13′): } H_4(\xi_2) = P_c\left(1 - \frac{\xi_2}{L}\right) \qquad (0 \le \xi_2 \le L) \tag{7.36}$$

where $L = \sqrt{(P_a^2 + P_b^2)}$.

The yarn orientation angles α, β and γ in Fig. 7.24 are defined as

$$\begin{aligned} \alpha &= \tan^{-1}\sqrt{\left(\frac{P_b^2 + P_c^2}{P_a}\right)} \\ \beta &= \tan^{-1}\frac{P_b}{P_a} \\ \gamma &= \tan^{-1}\frac{P_c}{L} \end{aligned} \tag{7.37}$$

With the above geometrical relations and assumptions, the three-dimensional braided composite of Fig. 7.24 can be modeled based upon the classical lamination theory. The approach is essentially an extension of the fiber crimp model of Section 6.5. Thus, the constitutive equations of a laminated plate follow Eq. (6.1). The stiffness constants, Q_{ij}, are given by Eq. (6.10).

Since the undirectional yarns in each of the four laminae of Fig. 7.29 are at an angle, γ, with respect to the ξ-direction (see Fig. 7.24b), the effective elastic properties of lamina 1 in the ξ–ζ plane,

for example, are given by Eq. (6.74) as

$$
\begin{aligned}
E_{\xi\xi}(\gamma) &= \left(\frac{\cos^4\gamma}{E_{11}} + \left(\frac{1}{G_{12}} - \frac{2\nu_{21}}{E_{22}}\right)\cos^2\gamma\sin^2\gamma + \frac{\sin^4\gamma}{E_{22}}\right)^{-1} \\
E_{\zeta\zeta}(\gamma) &= E_{22} = E_{33} \\
G_{\xi\zeta}(\gamma) &= \left(\frac{\cos^2\gamma}{G_{12}} + \frac{\sin^2\gamma}{G_{23}}\right)^{-1} \\
\nu_{\zeta\xi}(\gamma) &= \nu_{21}\cos^2\gamma + \nu_{32}\sin^2\gamma
\end{aligned}
\tag{7.38}
$$

The transverse isotropy in the plane perpendicular to the yarn direction has been taken into account. Then the stiffness matrix, $Q_{ij}(\gamma)$, similar to Eq. (6.25) can be written in terms of $E_{\xi\xi}$, $E_{\zeta\zeta}$, $G_{\xi\zeta}$, $\nu_{\zeta\xi}$, and $D_\gamma = 1 - \nu^2_{\zeta\xi}(\gamma)E_{\xi\xi}(\gamma)/E_{\zeta\zeta}$.

For lamina 1, the yarn segments in an inclined lamina also form an off-axis angle, β, with respect to the braiding direction (x axis). Thus, the effective laminar elastic properties in the x direction are

Fig. 7.29. Four unidirectional laminae representing the inclined yarns. (After Yang, Ma and Chou 1986.)

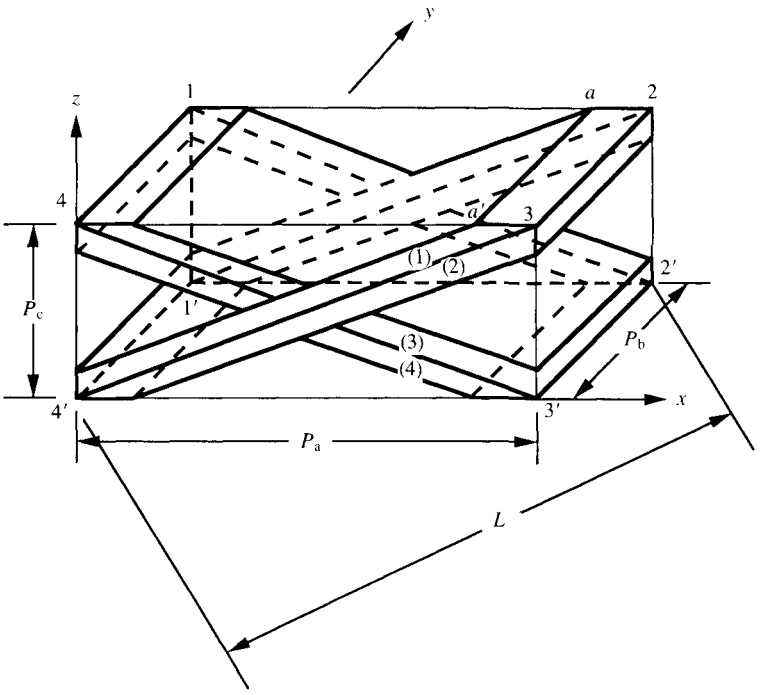

further reduced, and the stiffness constants of the laminae become

$$\bar{Q}_{ij}(\beta, \gamma) = \begin{bmatrix} \bar{Q}_{11} & \bar{Q}_{12} & \bar{Q}_{16} \\ \bar{Q}_{12} & \bar{Q}_{22} & \bar{Q}_{26} \\ \bar{Q}_{16} & \bar{Q}_{26} & \bar{Q}_{66} \end{bmatrix} \tag{7.39}$$

where

$$\begin{aligned}
\bar{Q}_{11} &= \left[\frac{E_{\xi\xi}(\gamma)}{D_\gamma}\right]\cos^4\beta + 2\left[\frac{E_{\xi\xi}(\gamma)\nu_{\zeta\xi}(\gamma)}{D_\gamma} + 2G_{\xi\zeta}(\gamma)\right] \\
&\quad \times \cos^2\beta \sin^2\beta + \left[\frac{E_{\zeta\zeta}}{D_\gamma}\right]\sin^4\beta \\
\bar{Q}_{12} &= \left[\frac{E_{\xi\xi}(\gamma)}{D_\gamma} + \frac{E_{\zeta\zeta}}{D_\gamma} - 4G_{\xi\zeta}(\gamma)\right]\cos^2\beta \sin^2\beta \\
&\quad + \left[\frac{E_{\xi\xi}(\gamma)\nu_{\zeta\xi}(\gamma)}{D_\gamma}\right][\cos^4\beta + \sin^4\beta] \\
\bar{Q}_{16} &= \left[\frac{E_{\xi\xi}(\gamma)}{D_\gamma} + \frac{E_{\xi\xi}(\gamma)\nu_{\zeta\xi}(\gamma)}{D_\gamma} - 2G_{\xi\zeta}(\gamma)\right]\cos^3\beta \sin\beta \\
&\quad + \left[\frac{E_{\xi\xi}(\gamma)\nu_{\zeta\xi}(\gamma)}{D_\gamma} - \frac{E_{\zeta\zeta}}{D_\gamma} + 2G_{\xi\zeta}(\gamma)\right]\cos\beta \sin^3\beta \\
\bar{Q}_{22} &= \left[\frac{E_{\xi\xi}(\gamma)}{D_\gamma}\right]\sin^4\beta + 2\left[\frac{E_{\xi\xi}(\gamma)\nu_{\zeta\xi}(\gamma)}{D_\gamma} + 2G_{\xi\zeta}(\gamma)\right] \\
&\quad \times \cos^2\beta \sin^2\beta + \left[\frac{E_{\zeta\zeta}}{D_\gamma}\right]\cos^4\beta \\
\bar{Q}_{26} &= \left[\frac{E_{\xi\xi}(\gamma)}{D_\gamma} - \frac{E_{\xi\xi}(\gamma)\nu_{\zeta\xi}(\gamma)}{D_\gamma} - 2G_{\xi\zeta}(\gamma)\right]\cos\beta \sin^3\beta \\
&\quad + \left[\frac{E_{\xi\xi}(\gamma)\nu_{\zeta\xi}(\gamma)}{D_\gamma} - \frac{E_{\zeta\zeta}}{D_\gamma} + 2G_{\xi\zeta}(\gamma)\right]\cos^3\beta \sin\beta \\
\bar{Q}_{66} &= \left[\frac{E_{\xi\xi}(\gamma)}{D_\gamma} + \frac{E_{\zeta\zeta}}{D_\gamma} - 2\frac{E_{\xi\xi}(\gamma)\nu_{\zeta\xi}(\gamma)}{D_\gamma} - 2G_{\xi\zeta}(\gamma)\right] \\
&\quad \times \cos^2\beta \sin^2\beta + G_{\xi\zeta}(\gamma)[\cos^4\beta + \sin^4\beta]
\end{aligned} \tag{7.40}$$

Knowing the effective laminae properties with respect to the x–y coordinate system, the local plate stiffness matrices $A_{ij}(x)$, $B_{ij}(x)$ and $D_{ij}(x)$ can be calculated from the lamination theory:

$$[(A_{ij}(x), B_{ij}(x), D_{ij}(x)] = \sum_{m=1}^{n} \int_{h_{m-1}}^{h_m} \bar{Q}_{ij}(\beta, \gamma)[1, z, z^2]\, dz \tag{7.41}$$

The integration is performed through the thickness of the unit cell of Fig. 7.29. By neglecting the contribution of the pure matrix region, the extensional stiffness matrix $A_{ij}(x)$, for instance, can be evaluated as follows:

$$A_{ij}(x) = \int_{H_1(\xi_1)}^{H_1(\xi_1)+h'} \bar{Q}_{ij}^{(1)}(\beta, \gamma)\,\mathrm{d}z + \int_{H_2(\xi_2)-h'}^{H_2(\xi_2)} \bar{Q}_{ij}^{(2)}(\beta, \gamma)\,\mathrm{d}z + \int_{H_3(\xi_1)}^{H_3(\xi_1)+h'} \bar{Q}_{ij}^{(3)}(\beta, \gamma)\,\mathrm{d}z + \int_{H_4(\xi_2)-h'}^{H_4(\xi_2)} \bar{Q}_{ij}^{(4)}(\beta, \gamma)\,\mathrm{d}z \tag{7.42}$$

where the superscripts (1), (2), (3) and (4) correspond to the laminae in Fig. 7.29. Also, $h' = h/\cos\gamma$, where h is the thickness of a lamina. It should be noted that the signs of the angles β and γ of the laminae 2, 3 and 4 depend on the fiber orientations. In order to avoid over-estimation of the composite properties, the portions of the laminae which lie outside of the unit cell (such as the region above $aa'32$ in Fig. 7.29) have been excluded from the integration in Eq. (7.41). The lamina thickness is so determined that the total cross-sectional area of laminae (1), (2), (3) and (4) in the x–z plane is equal to that of the unit cell.

The inversion of the local stiffness matrices $A_{ij}(x)$, $B_{ij}(x)$ and $D_{ij}(x)$ of Eq. (7.41) yields the local laminate compliance matrices $A'_{ij}(x)$, $B'_{ij}(x)$ and $D'_{ij}(x)$. The average in-plane compliances of the unit cell under a uniformly applied in-plane stress resultant are

$$\begin{aligned} \bar{A}'_{ij} &= \frac{1}{P_a}\int_0^{P_a} A'_{ij}(x)\,\mathrm{d}x \\ \bar{B}'_{ij} &= \frac{1}{P_a}\int_0^{P_a} B'_{ij}(x)\,\mathrm{d}x \\ \bar{D}'_{ij} &= \frac{1}{P_a}\int_0^{P_a} D'_{ij}(x)\,\mathrm{d}x \end{aligned} \tag{7.43}$$

Then, the averaged stiffness matrices $\bar{A}_{ij}$, $\bar{B}_{ij}$, and $\bar{D}_{ij}$ for the unit cell can be obtained by the inversion of $\bar{A}'_{ij}$, $\bar{B}'_{ij}$, and $\bar{D}'_{ij}$. Finally, effective laminate engineering constants E_{xx}, E_{yy}, ν_{xy} and G_{xy} can be expressed as functions of the stiffness constants $\bar{A}_{ij}$ and the unit cell thickness.

Figures 7.30 and 7.31 show the comparisons of theoretical calculations for the axial Young's modulus and Poisson's ratio with experimental data for three-dimensional braided carbon/epoxy composites (Yang, Ma and Chou 1986). The basic material

properties are $E_f = 234.4$ GPa and $\nu_f = 0.22$ for Celion 12K carbon fiber, and $E_m = 3.4$ GPa and $\nu_m = 0.34$ for epoxy matrix. The average yarn angle in the braided preform is denoted by α.

As the braiding angle becomes smaller, the performance of the inclined laminae approaches that of the unidirectional laminae. The interchange of the stacking sequence of the four inclined laminae in the unit cell does not affect the effective in-plane properties. The

Fig. 7.30. Predicted axial elastic moduli of three-dimensional braided composites as functions of fiber volume fraction, V_f, and fiber orientation angle, α. ●, ▲, ■ and ×: experimental data. (After Yang, Ma and Chou, 1986.)

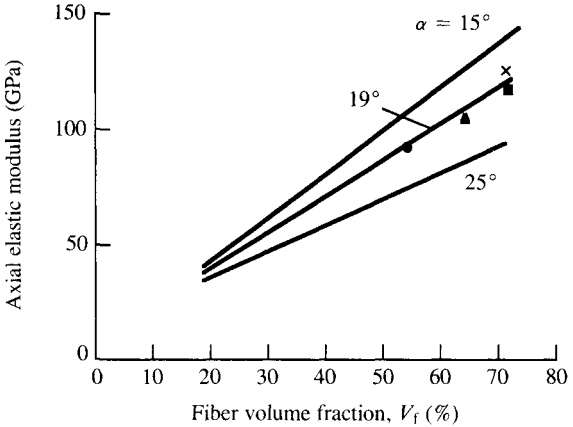

Fig. 7.31. Predicted Poisson's ratios of three-dimensional braided composites as functions of fiber volume fraction, V_f, and fiber orientation angle, α. ●, ■, and ×: experimental data. (After Yang, Ma and Chou, 1986.)

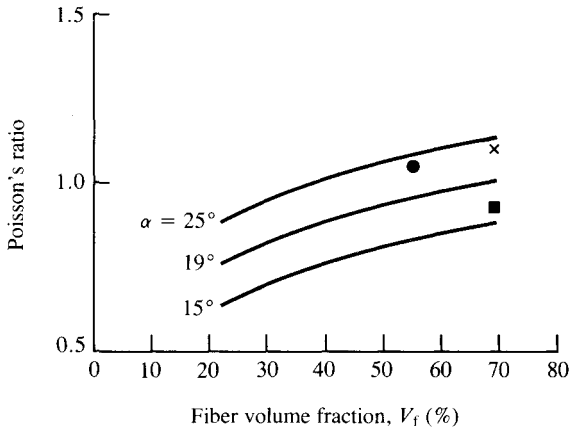

Poisson's ratio of three-dimensional composites based upon 4-step braiding is considerably higher than that of a unidirectional composite with the same fiber volume fraction. The Poisson's contraction can be minimized by introducing laid-in yarns in the axial direction.

7.5.3 *Macro-cell approach*

The approach of the macro-cell model is different from that of the unit cell. Instead of considering the smallest repeating unit in a preform, the macro-cell is established for the entire cross-section of the specimen. It takes into account the arrangements of the yarns around the edges of the specimen. However, the most distinct advantage of this approach perhaps is its capability of dealing with specimens of 'thick' cross-sections, since the elastic properties are derived from tensor transformations. In order to apply such a model, it is necessary to have detailed knowledge of the fiber geometric configurations.

In the following, the macro-cell model (Byun, Du and Chou 1991) is applied to the analysis of elastic properties of 2-step braided fabric composites. The treatment is excerpted from Byun, Whitney, Du and Chou (1991).

7.5.3.1 *Geometric relations*

Consider the 2-step braided composite depicted in Fig. 7.17. The variation in the braider yarn orientation along its length is taken into account by introducing the average yarn orientation angle. The average is identified by considering one braider yarn which travels through the length of the macro-cell. For an m-column by n-layer braided preform, a braider yarn travels $m + (n + 1)/2$ pitch lengths before it repeats its spatial position. Thus, for the preform of Fig. 7.17 the repeating length is ten pitch lengths. Figure 7.32 shows the schematic view of the braider yarn location and

Fig. 7.32. Schematic view of a braider yarn extending through ten pitch lengths. The numbers indicate the braider yarn carrier locations in Fig. 7.3. (After Byun *et al.* 1991.)

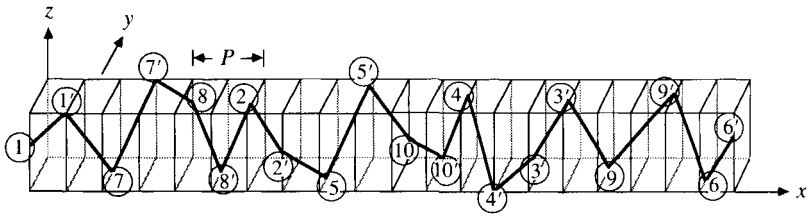

orientation; the numbers indicate the positions of braider yarn carriers in Fig. 7.3.

In order to identify the reinforcing direction of braider yarns, the yarn segments generated due to the carrier movement from position 1 to 7′ in Fig. 7.32 are projected onto the y–z (Fig. 7.33) and z–x (Fig. 7.34) planes. Thus, all the yarn segments are identified according to their directions with respect to the x–y–z coordinate. L_{bi}, L_{by} and L_{bz} denote the total projected length of braider yarns which are inclined to the x, y and z axes, parallel to the x–y plane, and parallel to the z–x plane, respectively. Then, from Fig. 7.17 and the parameters defined in Eqs. (7.12)–(7.14),

$$L_{bi} = 4(m-1)(n-1)\left(S_a + \frac{S_b f_b}{\sin 2\theta}\right) \tag{7.44}$$

$$L_{by} = 2[(n-1)S_m + 2(m-1)S_a \cos\theta] \tag{7.45}$$

$$L_{bz} = 2[2mS_n + (n-1)S_a \sin\theta] \tag{7.46}$$

where m and n denote the column and layer numbers, respectively.

Fig. 7.33 Projections of the yarn segment 11′77′ of Fig. 7.32 onto the y–z plane. (After Byun *et al.* 1991.)

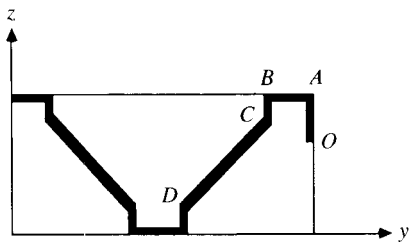

Fig. 7.34. Projections of the yarn segment 11′77′ of Fig. 7.32 onto the x–z plane. (After Byun *et al.* 1991.)

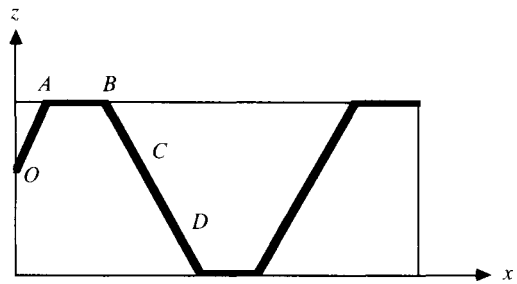

The average angle between the braider yarn and the braid axis is given by

$$\bar{\alpha} = \tan^{-1}\left(\frac{2L_t}{(2m+n+1)P}\right) \tag{7.47}$$

where $L_t (= L_{bi} + L_{by} + L_{bz})$ is the projected length of the braider yarn onto the y–z plane. Based upon the average braider yarn orientation angle, the total length of braider yarn (L_b) is approximated as

$$L_b = \frac{L_t}{\sin\bar{\alpha}} \tag{7.48}$$

The lengths of braider yarns inclined to the xyz axes and parallel to the x–y and z–x planes can be obtained in a similar manner. Thus the volumes of braider yarns of these three orientations are given by

$$\begin{aligned} V_{bi} &= S_b^2 f_b (L_{bi}/\sin\bar{\alpha}) \\ V_{by} &= S_b^2 f_b (L_{by}/\sin\bar{\alpha}) \\ V_{bz} &= S_b^2 f_b (L_{bz}/\sin\bar{\alpha}) \end{aligned} \tag{7.49}$$

The axial yarns have three different cross-sections as shown in Fig. 7.17. The total volume of the axial yarns is

$$\begin{aligned} V_a = h[&(m-1)(n-1)S_a^2 \sin(2\theta) + 4(m-1)S_a S_n \cos\theta \\ &+ 2(n-1)S_a S_m \sin\theta + 4S_m S_n] \end{aligned} \tag{7.50}$$

Using Eqs. (7.15) and (7.16), the total macro-cell volume is

$$V_t = wt \tag{7.51}$$

The fiber volume fractions of braider yarns of different orientations can therefore be obtained from Eqs. (7.49)–(7.51); they are used for evaluating the volume average of the stiffness constants.

7.5.3.2 *Elastic constants*

For the purpose of predicting the composite elastic properties, the yarns are treated as unidirectional composite rods. The direction cosines between the reference coordinate system, xyz, and the 123 coordinate system associated with the unidirectional composite can be established by setting the 2 axis perpendicular to the z axis (Fig. 7.35):

$$\begin{aligned} l_{1x} &= \cos\beta\cos\gamma & l_{2x} &= -\sin\beta & l_{3x} &= -\cos\beta\sin\gamma \\ l_{1y} &= \sin\beta\cos\gamma & l_{2y} &= \cos\beta & l_{3y} &= -\sin\beta\sin\gamma \\ l_{1z} &= \sin\gamma & l_{2z} &= 0 & l_{3z} &= \cos\gamma \end{aligned} \tag{7.52}$$

Considering the average angle of braider yarn $\bar{\alpha}$ instead of α in Fig. 7.35, the angles β and γ can be expressed in terms of $\bar{\alpha}$ and the aspect ratio of axial yarns, f_a, as

$$\beta = \tan^{-1}[\cos\theta \tan\bar{\alpha}] = \tan^{-1}\left[\frac{\tan\bar{\alpha}}{\sqrt{(1+f_a^2)}}\right] \tag{7.53}$$

$$\gamma = \tan^{-1}\left[\frac{\sin\theta}{\sqrt{(\cot^2\bar{\alpha}+\cos^2\theta)}}\right] = \tan^{-1}\left[\frac{f_a\sin\bar{\alpha}}{\sqrt{(1+f_a^2\cos^2\bar{\alpha})}}\right] \tag{7.54}$$

Using these direction cosines, the compliance matrix (S) of the unidirectional composite (OO′ in Fig. 7.35) referring to the 123 coordinate system can be transformed to that referring to the xyz coordinate system:

$$S'_{ijmn} = l_{pi}l_{qj}l_{rm}l_{sn}S_{pqrs} \qquad (i, j, m, n, p, q, r, s = 1, 2, 3) \tag{7.55}$$

From symmetry conditions and using contracted notation, Eq. (7.55) is reduced to a simple form:

$$S'_{ij} = q_{mi}q_{nj}S_{mn} \qquad (i, j, m, n = 1\text{–}6) \tag{7.56}$$

where q_{ij} denotes the element belonging to the ith row and jth column of the transformation matrix (see Lekhnitskii 1963). For a unidirectional composite with transverse isotropy, the compliance matrix has five independent constants.

In order to determine the effective stiffness matrix of the composite, the compliance matrix is inverted and then averaged

Fig. 7.35. Orientation of the braider yarn (OO′). (After Byun *et al.* 1991.)

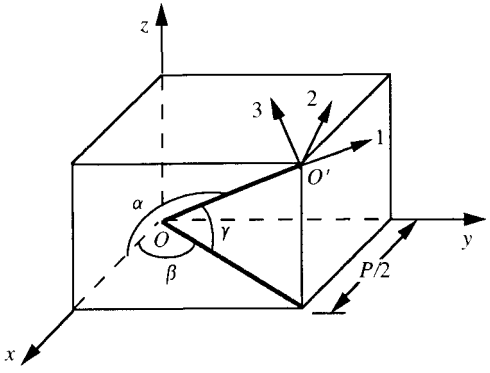

over the macro-cell volume. The average should include all four yarn orientations in Fig. 7.33, namely the axial yarn ($\beta = 0$, $\gamma = 0$), braider yarn (BA) parallel to the x–y plane ($\beta = \bar{\alpha}$, $\gamma = 0$), braider yarn (BC) parallel to the z–x plane ($\beta = 0$, $\gamma = \bar{\alpha}$) and inclined braider yarn (CD) in the interior of the macro-cell ($\beta = f(\bar{\alpha}, f_a)$, $\gamma = g(\bar{\alpha}, f_a)$). Thus, the effective stiffness of the composite C_{ij}^c is

$$C_{ij}^c = \sum_{n=1}^{4} (C_{ij})_n \frac{V_n}{V_t} \tag{7.57}$$

where $(C_{ij})_n$ and V_n/V_t are, respectively, the stiffness matrix and volume fraction of the unidirectional composite for an individual reinforcing direction. Finally, the stiffness matrix of the composite is inverted to obtain the compliance matrix S_{ij}^c. The engineering elastic constants are then obtained from the compliance matrix. For example, $E_{xx} = 1/S_{11}^c$, $E_{yy} = 1/S_{22}^c$ and $\nu_{xy} = -S_{12}^c/S_{22}^c$, etc.

Experimental measurements of the elastic properties of 2-step braided composites have been reported by Byun *et al.* (1991). The composites are the same as for Braid II given in Table 7.1. Experimental observations of specimen cross-section confirm the yarn shapes assumed in the analysis. Based upon the input data of Table 7.1, the macro-cell model predicts the following composite geometric parameters: thickness (t) = 7.1 mm, width (w) = 15.3 mm, average braider angle ($\bar{\alpha}$) = 71.1° and fiber volume fraction (V_f) = 73.2%. Table 7.2 shows the comparison of elastic properties based upon the macro-cell predictions and experiments.

Table 7.2. *Comparisons of composite elastic properties from the macro-cell model predictions and experiments. After Byun et al.* (1991).

Elastic constants	Macro-cell model	Experiment
E_{xx} (GPa)	48.4	52.4 (5*)
E_{yy} (GPa)	7.83	
E_{zz} (GPa)	7.95	
G_{xy} (Gpa)	2.58	1.45 (4*)
G_{yz} (GPa)	2.68	
G_{xz} (GPa)	2.59	
ν_{xy}	0.33	0.53 (3*)
ν_{yz}	0.35	
ν_{xz}	0.36	

* Number of tests.

The analytical predictions deviate significantly from experimental results for the in-plane shear modulus and Poisson's ratio. Some reasons of uncertainty in the measurements of fabric composite elastic properties are discussed in Section 7.7.

7.6 Structure–performance maps of composites

Considerable effort has been devoted by researchers to evaluate the effectiveness of various reinforcement concepts. However, the analyses and experiments performed on advanced composites are usually reported for individual systems; it is thus difficult to acquire a more comprehensive view. Chou and Yang (1986) and Chou (1989), motivated by the concept of deformation mechanism maps of Ashby, Gandi and Taplin (1979), Gandi and Ashby (1979) and Frost and Ashby (1982) as well as the work of Dow (1984) have integrated the results of studies in the modeling of thermoelastic behavior of unidirectional laminated composites, as well as two-dimensional (2-D) and three-dimensional (3-D) textile structural composites. Through the construction of structure–performance maps, the relative effectiveness and uniqueness of various reinforcement concepts can be assessed. These maps provide guidance in material selection for structural design, and in identifying the needs of future work.

In order to assess the capability of various reinforcement configurations with different fibers and matrix combinations, Chou and Yang conducted parametric studies of the structure–performance relationship. The geometric parameters considered include fiber orientation in unidirectional laminated constructions, weaving parameters in two-dimensional fabrics, and braiding parameters in three-dimensional constructions. The material parameters are fiber and matrix thermoelastic properties. Four types of reinforcement forms are presented below: laminated angle-plies based upon unidirectional layers with the off-axis angle (θ) ranging from 0° to 90°; [0°/90°] cross-plies; two-dimensional woven fabrics with n_g ranging from 2 (plain weave) to 8 (eight-harness satin); and 2-step and 4-step braided composites. For 2-step braids, yarn linear density, pitch length and aspect ratio are allowed to change. The braiding angle between a fiber segment and braiding axis in the case of 4-step braids varies from 15° to 35°. The analytical tools employed in the construction of these maps include the lamination theory for cross-ply and angle-ply laminates, the crimp and bridging models (Chapter 6) for two-dimensional fabrics, the fiber

inclination model for 4-step braided composites, and the macro-cell model for 2-step braided composites.

Several maps are presented here to illustrate the correlation between reinforcement configurations and the thermoelastic behavior of composites. The fiber volume fractions of the composites are assumed to be 73% for 2-step braided composites and 60% for all other composites. Figures 7.36–7.39 present the thermoelastic behavior of carbon, Kevlar and glass reinforced epoxy composites. Figure 7.40 shows the variation of thermal expansion coefficients for PEEK matrix composites. Figure 7.41 gives the elastic properties of C, SiC and Al_2O_3 fiber reinforced Mg matrix composites. Figure 7.42 demonstrates the elastic properties of glass matrix composites reinforced with C, SiC and Al_2O_3 fibers. The three-dimensional

Fig. 7.36. E_{xx} vs. E_{yy} for carbon/epoxy (■ unidirectional angle-ply; △ two-dimensional woven; + three-dimensional braided), Kevlar/epoxy (▲ unidirectional angle-ply; □ two-dimensional woven; × three-dimensional braided), and glass/epoxy (● unidirectional angle-ply; ○ two-dimensional woven; ▼ three-dimensional braided) composites. (p) = plain weave; (s) = eight-harness satin. (After Chou and Yang 1986.)

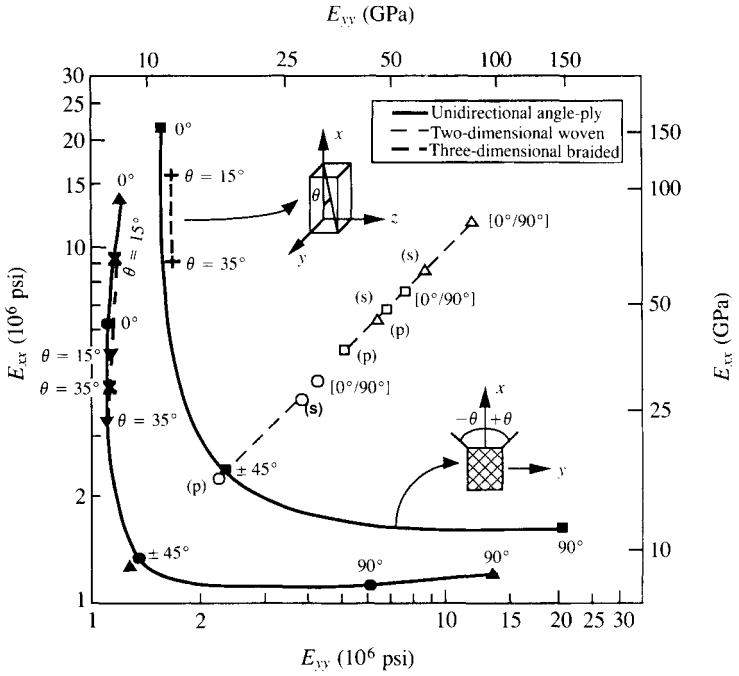

preforms discussed in Figs. 7.36–7.42 are based upon 4-step braiding.

Figures 7.43 and 7.44 show the variations of elastic properties of 2-step braided composites of Kevlar/epoxy with fabric geometric and processing parameters. The linear density ratio of axial and braider yarns, the pitch length of braider yarns, and the aspect ratios of axial and braider yarns are considered. The structure–performance maps are constructed by starting with a set of values of these parameters, and then varying each parameter independently while keeping the other parameters at their original values. The ranges of these values are denoted on the curves in Figs. 7.43 and

Fig. 7.37. E_{xx} vs G_{xy} for carbon/epoxy (■ unidirectional angle-ply; △ two-dimensional woven; + three-dimensional braided), Kevlar/epoxy (▲ unidirectional angle-ply; □ two-dimensional woven; × three-dimensional braided), and glass/epoxy (● unidirectional angle-ply; ○ two -dimensional woven; ▼ three-dimensional braided) composites. (p) = plain weave; (s) = eight-harness satin. (After Chou and Yang 1986.)

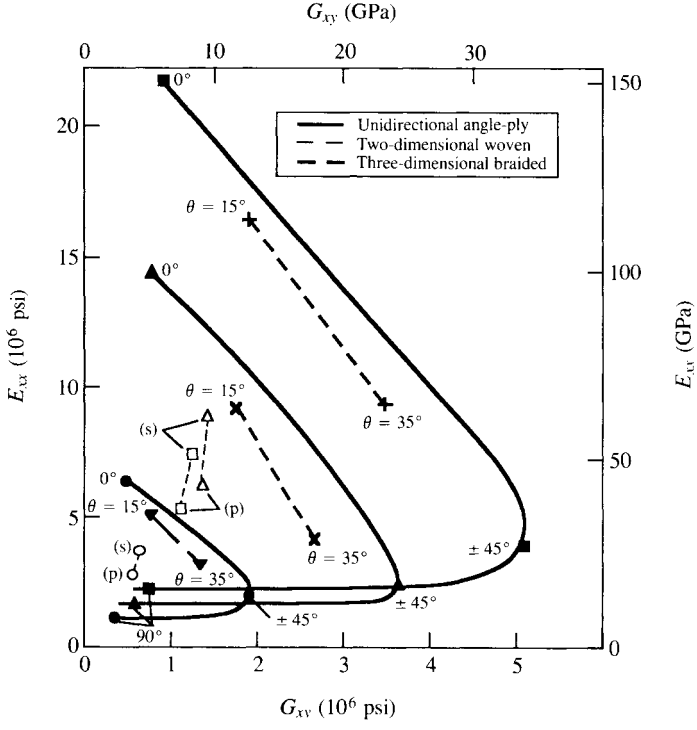

7.44 where the calculations are performed at equal intervals as indicated by the symbols on each curve (Byun *et al.* 1991).

It is noted from Figs. 7.43 and 7.44 that the Young's moduli and shear moduli are insensitive to the axial yarn aspect ratios between 1 and 3. The maximum volume fraction of axial yarns is achieved when the yarn aspect ratio is around unity, which also gives the maximum E_{xx} and G_{yz}. Increases in the linear density ratio of axial yarn to braider yarn result in an increase in axial yarn volume fractions while the braider yarn volume fraction becomes smaller.

Since the stiffness increases of the 2-step braided composite in the longitudinal and transverse directions are primarily due to the contribution of the axial yarns and braider yarns, respectively, the increase of the axial yarn volume fraction improves E_{xx}. In the meantime, E_{yy} and G_{yz} become smaller due to the reduction in braider yarn volume fraction. Furthermore, the increase in the aspect ratio of the braider yarns results in an increase in their thickness, which in turn gives a larger volume of matrix pockets in the composite. Since the total fiber volume fraction is reduced due to

Fig. 7.38. E_{xx} vs. ν_{xy} for carbon/epoxy (■ unidirectional angle-ply, △ two-dimensional woven, + three-dimensional braided) composites. (After Chou and Yang 1986.)

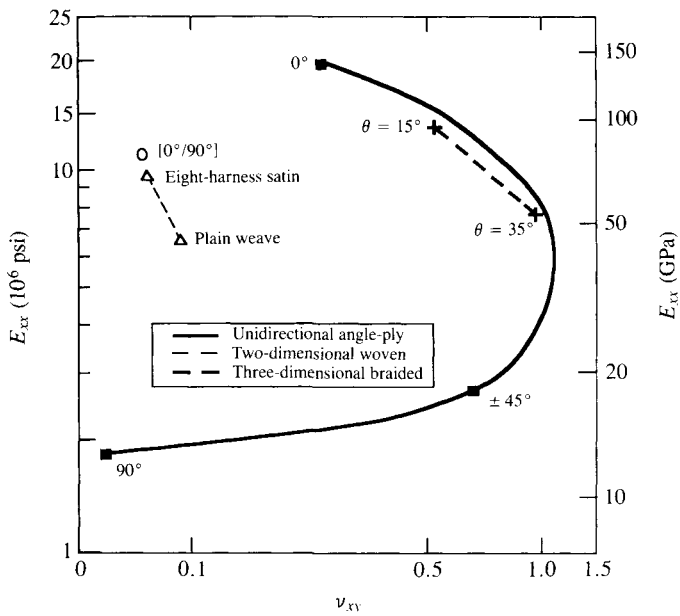

the increase in volume of the composite, all the components of Young's moduli and shear moduli in Figs. 7.43 and 7.44 are reduced as the braider yarn aspect ratio becomes bigger. Finally, longer braider yarn pitch length gives a small volume fraction and orientation angle of braider yarns. Consequently, E_{yy} and G_{yz} are reduced as the braider yarn pitch length increases.

Chou and Yang (1986) have compared the unique thermal and elastic characteristics among various reinforcement configurations. In general, the in-plane thermoelastic properties of unidirectional lamina depend strongly on the fiber orientation. The unidirectional reinforcement provides the highest elastic stiffness along the fiber direction. The Young's moduli of off-axis unidirectional laminae are lower than that of the unidirectional lamina.

The [0°/90°] cross-ply yields identical thermoelastic properties in 0° and 90° orientations. Their in-plane shear rigidity is poor. The longitudinal Young's modulus of an angle-ply laminate is lower than

Fig. 7.39. α_{xx} vs. α_{yy} for carbon/epoxy (■ unidirectional angle-ply; △ two-dimensional woven; + three-dimensional braided), Kevlar/epoxy (▲ unidirectional angle-ply; □ two-dimensional woven; × three-dimensional braided), and glass/epoxy (● unidirectional angle-ply; ○ two-dimensional woven; ▼ three-dimensional braided) composites. (p) = plain weave; (s) eight-harness satin. (After Chou and Yang 1986.)

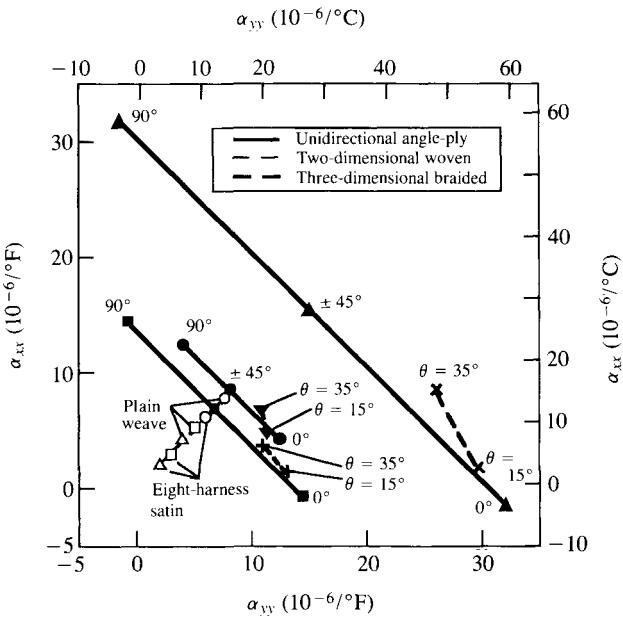

that of a unidirectional lamina. But better transverse elastic property and in-plane shear resistance can be achieved through the stacking of the unidirectional laminae with different fiber orientations. For ±45° angle-ply, the in-plane stiffness drops to a minimum, while the shear modulus reaches its maximum.

The two-dimensional biaxial woven fabric composites can provide balanced in-plane thermoelastic properties within a single ply. They behave similar to [0°/90°] cross-plies, although the fiber waviness tends to reduce the in-plane efficiency of the reinforcements. As the fabric construction changes from plain weave to eight-harness satin, the frequency of crimp due to fiber cross-over is reduced, and the fabric structure approaches that of [0°/90°] cross-plies.

The thermoelastic properties of braided composites also show a strong dependence on fiber orientation. Three-dimensionally braided composites have demonstrated good in-plane properties, which are comparable to those of unidirectional angle-plies with the

Fig. 7.40. α_{xx} vs. α_{yy} for carbon/PEEK (■ unidirectional angle-ply; △ two-dimensional woven; + three-dimensional braided), Kevlar/PEEK (▲ unidirectional angle-ply; □ two-dimensional woven; × three-dimensional braided), and glass/PEEK (● unidirectional angle-ply; ○ two-dimensional woven; ▼ three-dimensional braided) composites. (After Chou and Yang 1986.)

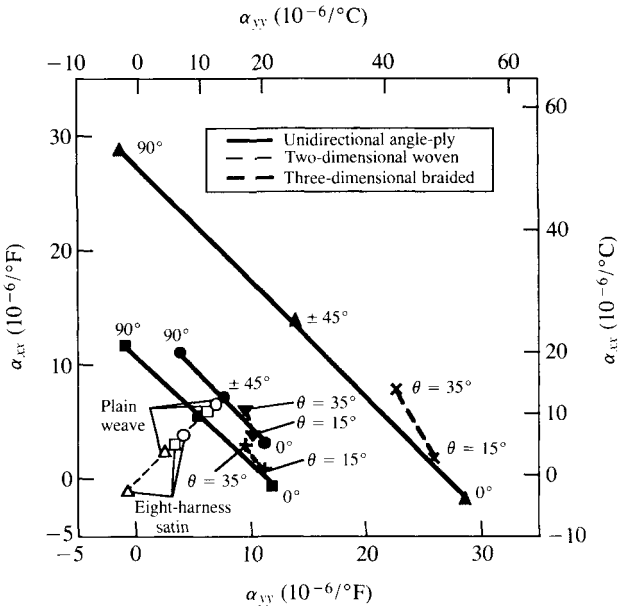

same range of fiber orientation. The longitudinal Young's moduli and in-plane shear rigidities of three-dimensional braided composites with braiding angles ranging from 15° to 35° are better than those of two-dimensional woven fabric composites. But the transverse Young's moduli are lower and the major Poisson's ratios higher than those of two-dimensional woven fabric composites. However, three-dimensional braided composites are unique in providing both stiffness and shear rigidity along the thickness direction. Also, because of the integrated nature of the fiber arrangement, there are no interlaminar surfaces in three-dimensional composites.

Furthermore, a comparison of their elastic behavior indicates that the performance of 2-step braided composites is much more versatile than that of 4-step braided composites. The presence

Fig. 7.41. E_{xx} vs. E_{yy} carbon/magnesium (● unidirectional angle-ply; △ two-dimensional woven; ▼ three-dimensional braided), SiC/magnesium (▲ unidirectional angle-ply; ○ two-dimensional woven; × three-dimensional braided), and Al_2O_3/magnesium (■ unidirectional angle-ply; □ two-dimensional woven; + three-dimensional braided) composites. (After Chou and Yang 1986.)

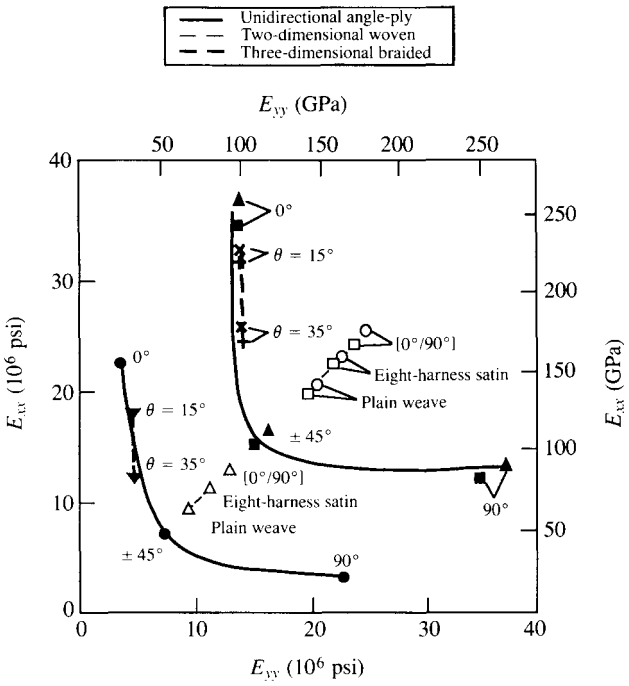

of both axial and braider yarns in 2-step braids allows much flexibility in the design of the preform microstructure. However, such flexibility can be achieved in 4-step braided composites if laid-in axial yarns are used.

The structure–performance maps can form the basis for material selection and component design; these findings can be easily extended to generate a wider range of information. Take the woven fabric composite as an example; although the properties shown in the maps are primarily along the filling and warp directions, the off-axis properties can be readily obtained through proper tensor transformation. Upon knowing these properties, it would be feas-

Fig. 7.42. E_{xx} vs. G_{xy} for carbon/borosilicate glass (● unidirectional angle-ply; △ two-dimensional woven; ▼ three-dimensional braided), SiC/borosilicate glass (■ unidirectional angle-ply; ○ two-dimensional woven; + three-dimensional braided), and Al_2O_3/borosilicate glass (▲ unidirectional angle-ply; □ two-dimensional woven; × three-dimensional braided) composites and three-dimensional carbon/carbon composites (◆). (After Chou and Yang 1986.)

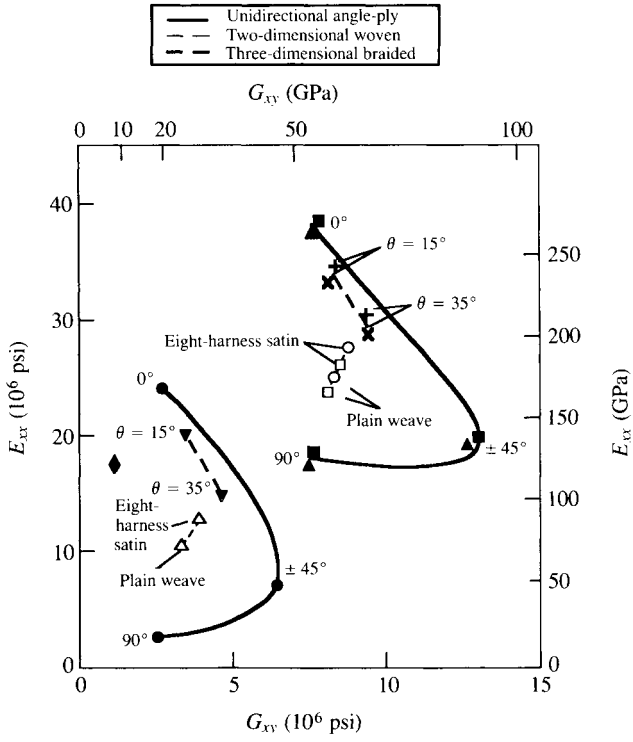

Fig. 7.43. The variations of E_{xx} and E_{yy} with material and processing parameters (intervals of the parameters, axial yarn aspect ratio: 1, pitch length:2, linear density ratio: 0.05, braider yarn aspect ratio: 0.02). (After Byun *et al.* 1991.)

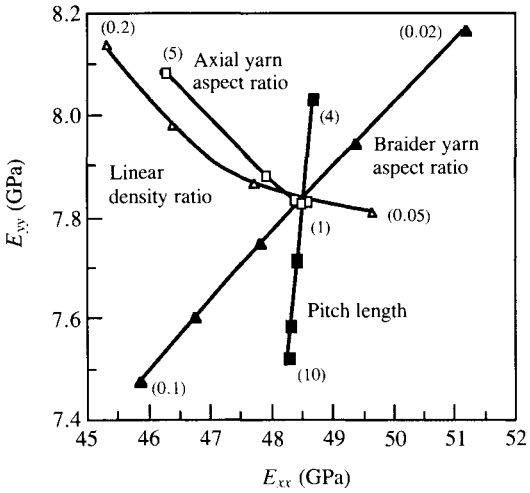

Fig. 7.44. The variations of G_{xy} and G_{yz} with material and processing parameters (intervals of the parameters, axial yarn aspect ratio: 1, pitch length: 2, linear density ratio: 0.05, braider yarn aspect ratio: 0.02). (After Byun *et al.* 1991.)

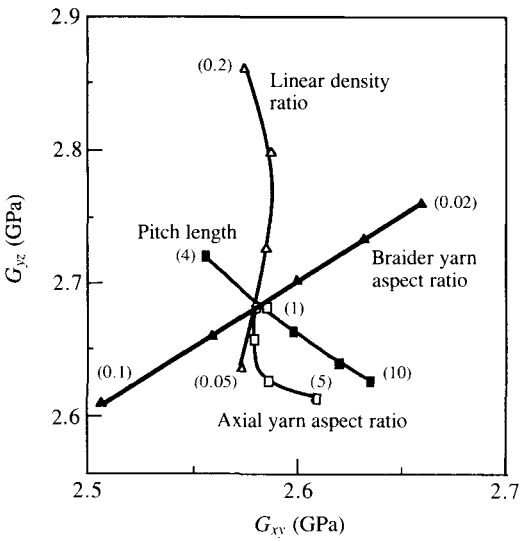

ible to tailor composite structures with various combinations of reinforcement forms, or with different material combinations such as hybrid unidirectional laminate, hybrid woven fabric structures, or hybrid laid-in three-dimensional structures.

It should be noted that the analytical modeling techniques employed in the construction of the structure–performance maps assume 'defect-free' composites, i.e. perfect fiber/matrix interfacial bonding, perfect fiber alignment, void-free matrix materials, etc. It is understood that in actual composites defects are frequently introduced in the fabrication and handling process. Limited studies in this regard have been made, including the effect of fabrication induced fiber distortion on the thermoelastic properties of two-dimensional fabric composites (Yang and Chou 1989), the effects of fiber/matrix interfacial debonding on the effective elastic properties (Takahashi and Chou 1986), void content of as-fabricated polymeric matrix composites (Yoshida, Ogasa and Hayashi 1986), cracking of polymeric matrices in fabric composites (Ishikawa and Chou 1982), and the effect of fiber bundle size and distribution on the behavior of three-dimensional braided Al_2O_3/Al–Li composites (Majidi, Yang and Chou 1986). It is expected that with the advancement in mathematical modeling and experimental techniques, performance maps for strength and failure of various two- and three-dimensional composites can also be constructed.

7.7 Mechanical properties of composites

This section summarizes the strength, fracture, and damage tolerance behavior of three-dimensional fabric composites. The material systems cited here include both polymer and metal based composites.

7.7.1 *Tensile and compressive behavior*

Majidi, Yang, Pipes and Chou (1985) examined the tensile and compressive behavior of 4-step braided composites of alumina fiber in an aluminum–lithium matrix. The continuous, polycrystalline α-alumina yarn (Fiber FP manufactured by the Du Pont Co.) contains 210 filaments of approximately 20 μm diameter. The properties of Fiber FP are: tensile strength = 1380 MPa, tensile modulus = 345–79 GPa, elongation to failure = 0.4%, density = 3.90 g/cm^3, and melting point = 2045°C (Dhingra, Champion and Krueger 1975). The aluminum matrix is alloyed with 2–3 wt% lithium for an enhanced chemical bond between the fiber and the matrix.

Figure 7.45 depicts the tensile stress–strain curves of FP/Al–Li composites of unidirectional laminates and three-dimensional braided composites at $V_f = 17\%$ and 36%; the tensile behavior of the pure Al–Li matrix is also given. A bilinear behavior is observed for all composites; the 'knees' on the stress–strain curves occur at about 0.02%. Yielding of the matrix appears to be responsible for the bilinearity. Since the bilinear behavior has also been observed in the unidirectional composites, it is believed to be a material property rather than an effect caused by the braided structure. The *in situ* strength of the matrix may well be higher than that measured for the bulk material. Such a phenomenon has been discussed by Kelly and Macmillan (1966). When the fiber spacing is very small ($\leq 10\,\mu$m), as is the case in the material studied by Majidi and colleagues, the yield stress of the matrix is controlled by the Orowan stress and it is higher than that of the bulk matrix. The yield stress and work hardening increase with decreasing spacing between the fibers. While the yield stress goes up, the strain at which the matrix starts yielding in the composite drops for very small fiber spacing (Kies 1962).

The ultimate tensile strengths of three-dimensional braided composites with a braiding angle of about 20° are 189 MPa and 383 MPa for $V_f = 17\%$ and 36%, respectively. These values are slightly lower than those predicted for ±20% angle-ply laminates of

Fig. 7.45. Axial tensile stress–strain responses of (a) unidirectional FP/Al–Li composite ($V_f = 0.50$), (b) three-dimensional FP/Al–Li composite ($V_f = 0.36$), and (c) the unreinforced matrix. (After Majidi and Chou 1987.)

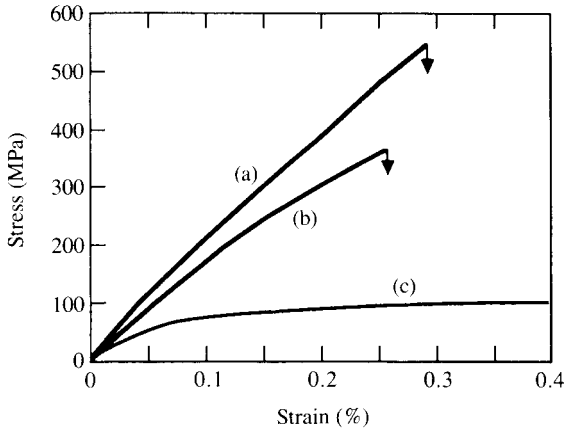

the same fiber volume fraction. Microscopic examination of the fracture surfaces reveals brittle fracture of fibers and considerable deformation in the matrix between the fibers.

The measured initial Young's moduli are 97 GPa and 171 GPa for $V_f = 17\%$ and 36%, respectively, which agree well with theoretical predictions based upon the fiber inclination model (Yang, Ma and Chou 1986). The secondary Young's moduli can be approximated by assuming that the contribution of the matrix to the composite modulus is negligible after yielding. The measured Poisson's ratios are 0.30 ($V_f = 17\%$) and 0.27 ($V_f = 36\%$). It should be noted that a certain degree of damage to brittle fibers often occurs in the braiding process. Thus, the *in situ* fiber stiffness and strength properties need to be estimated from, for instance, those measured on unidirectional composites.

Figure 7.46 shows the compressive stress–strain behavior of the same material as in Fig. 7.45(b). The curve demonstrates an initial linear region up to a strain of about 0.15% followed by nonlinear behavior. Other compressive properties include a failure strain of about 1.8% and a major Poisson's ratio of 0.3. Kinking appears to be the primary mode of failure in compression.

In transverse tension of three-dimensional braided FP/Al–Li composites the stress–strain curve is highly nonlinear. The onset of nonlinearity is at a strain of about 0.5%. The ultimate strength is

Fig. 7.46. Compressive stress–strain responses of FP/Al–Li composite. (After Majidi *et al.* 1985.)

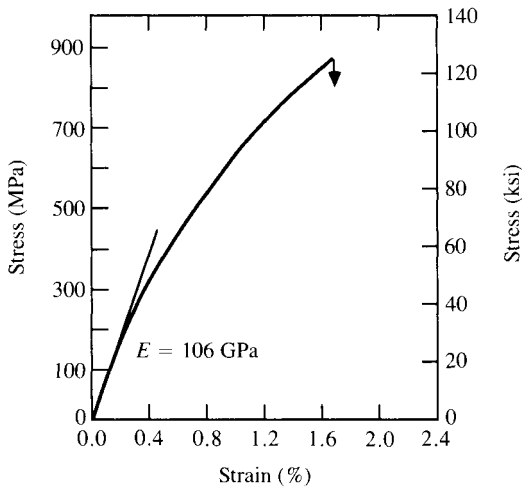

considerably lower than that for the axial specimen and, thus, significantly smaller than that of the unreinforced matrix material. Transverse cracks initiate within the matrix-rich regions between fiber bundles, most likely at microscopic voids in the matrix.

7.7.2 *Shear behavior*

Majidi *et al.* (1985) have examined the shear behavior of FP/Al–Li composites with a 4-step braided preform. Both intralaminar (in-plane) and interlaminar shear measurements are made. It has been shown that the short beam shear test (*ASTM Standards*, D2344-84 1987) causes premature failure by a flexural mode on the tensile surface of the specimen even for a fairly small specimen span-to-depth ratio. It is due to the high ratio of interlaminar shear strength to tensile strength in three-dimensional braided composites. The two-rail shear test (*ASTM Standards*, D4255-83 1987) also proved inadequate. The tests suitable for the measurement of the shear strength of three-dimensional composites are the Iosipescu shear test originally proposed by Iosipescu (1967) for isotropic materials and applied to composite laminates by Walrath and Adams (1983a&b), and the double-notch shear test.

The in-plane shear strength parallel to the braiding direction measured with the Iosipescu shear test for $V_f = 17\%$ is 139.6 MPa, which is comparable to the theoretical shear strength of 151 MPa for $[\pm 20°]$ angle-ply laminates of the same material and fiber volume fraction. Majidi, Rémond and Chou (1987) reported the shear properties of three-dimensional braided FP/Al–Li composite tubes, with the tube axis parallel to the braiding axis and braiding angles of approximately $\pm 20°$. The in-plane shear strengths measured from torsion tests are 141.8 MPa for $V_f = 17\%$ and 102.1 MPa for $V_f = 36\%$. The shear moduli are 36.6 GPa and 39.0 GPa for $V_f = 17\%$ and 36%, respectively.

The interlaminar shear strength measured by the double-notched shear test is 144.5 MPa. The calculated interlaminar shear strength for 0° unidirectional laminates is 100.8 MPa. This improved interlaminar shear property in the thickness direction of three-dimensional braided composites gives much improved fracture and impact resistance over the conventional laminates. Some dfficulties in the testing of three-dimensional textile structural composites exist. Machining of specimens should be avoided as much as possible because it destroys the integrated nature of the fiber preform and thus results in lower strength. It is also difficult to

obtain meaningful readings of the shear strain and, hence, shear modulus from the Iosipescu specimens. This is due to the relatively small size of the region of pure shear, the highly non-homogeneous three-dimensional braided structure based upon large bundles and the small size of the strain gages used. All these factors indicate the difficulties in the testing of textile structural composites in general.

7.7.3 *Fracture behavior*

7.7.3.1 *In-plane fracture*

The fracture and toughness characteristics of unidirectional and three-dimensional braided FP/Al–Li composites have been examined by Majidi, Yang and Chou (1986, 1988). Metal matrix composites, particularly those incorporating ceramic fibers, offer very high strength and stiffness, but often significantly lower fracture toughness than unreinforced metallic matrices. The reduced toughness is due to the restriction of plastic deformation in the presence of the stiff fibers and a strong fiber/matrix bond which eliminates or restricts fiber debonding and pullout.

Majidi and colleagues have measured fracture toughness using compact tension tests on the basis of the linear elastic fracture mechanics approach and the notched three-point bend test (Tattersal and Tappin 1966), which involves measurement of the work of fracture (fracture surface energy averaged over the whole fracture process).

Figures 7.47(a) and (b) show the load versus crack opening displacement (COD) curves for repeated loading and unloading of a three-dimensional braided composite and a unidirectional laminate under compact tension tests. The stress intensity factors are calculated from P_Q and the maximum load P_{max} indicated in Fig. 7.47(a). P_Q is determined by drawing a straight line with a slope 5% less than the slope of the linear part of the load–COD curve and finding the corresponding load at the intersection of this line with the curve. For Figs. 7.47(a) and (b), the crack propagation is perpendicular to the braiding axis of the three-dimensional braided composite and the fiber direction of the unidirectional laminate, respectively. In both cases, the first part of the load–COD curve is highly non-linear and, therefore, P_Q is considerably lower than P_{max}. For subsequent loading cycles, however, the sharpened crack removes the non-linearity in the curve and P_Q approaches P_{max}. Then, the stress intensity factors K_Q and K_{max} can be calculated

from P_Q and P_{max}, respectively (*Annual Book of ASTM Standards*, E399 1978). Since the K_{max} values are reasonably constant within the range of crack length to specimen width ratio, Majidi, Yang and Chou (1986) adopted the average K_{max} as the critical stress intensity factor, K_c. Rémond (1987) has characterized the fracture behavior of three-dimensional braided metal matrix composites with $V_f = 36\%$. For the notch perpendicular to the principal reinforcement axis, the unidirectional laminate ($K_{max} = 30.7\,MPa\sqrt{m}$) appeared tougher than the three-dimensional braided composite ($K_{max} = 27.3\,MPa\sqrt{m}$). For the notch parallel to the principal reinforcement axis, the three-dimensional braided composite ($K_{max} = 21.5\,MPa\sqrt{m}$) is tougher than the unidirectional laminate ($K_{max} = 19.0\,MPa\sqrt{m}$). The [±20°] angle-ply laminate appears less tough than the two other composites, the longitudinal toughness being $K_{max} = 24.6\,MPa\sqrt{m}$ and the transverse toughness $K_{max} = 16.4\,MPa\sqrt{m}$.

Electron microscopy investigations of the fracture surfaces indicate virtually no pull-out of the individual fibers. However, occasionally the whole fiber bundle has been pulled out over a small length of 1–2 mm. This is accompanied by some debonding between the fiber bundle and the surrounding matrix. The mechanism of crack propagation perpendicular to the braiding axis is believed to be the fracture of fibers and eventual fracture of the fiber bundle ahead of the crack tip. The above behavior differs greatly from that of the unidirectional FP/Al–Li composite, which shows a rapid

Fig. 7.47. Load–crack opening displacement (COD) curves obtained from compact tension tests on (a) three-dimensional braided FP/Al–Li composite ($V_f = 17\%$), and (b) unidirectional FP/Al–Li composite ($V_f = 34\%$). (After Majidi, Yang and Chou 1986.)

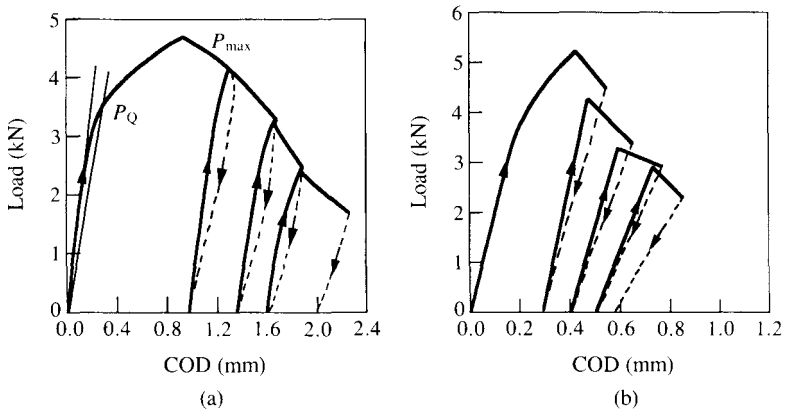

crack propagation from the outset and the fracture surface has a flat, brittle appearance with no macroscopic dimples.

In the case of notched three-point bend tests, unidirectional composites fracture in a much more brittle and less controlled manner than braided composites, and the load–deflection curve shows the sharp drop of load. The work of fracture, γ_f, which is measured from the total energy absorbed for the complete fracture of the specimen, or the area under the load–deflection curve, are $7.92 \pm 1.27\ \text{kJ/m}^2$ for the braided composites and $4.56 \pm 0.44\ \text{kJ/m}^2$ for unidirectional laminate for $V_f = 17\%$.

The difference in the strength and fracture behavior between textile structural composites and traditional laminated composites has been further demonstrated for the FP/Al–Li composites by Majidi, Yang and Chou (1986). In the case of unidirectional composites, the contributions from fiber debonding and pull-out are negligible since the critical load transfer length, l_c, is only 0.34 mm. This is calculated from the equation $l_c = \sigma_f d/(2\tau)$ where σ_f is the fiber ultimate strength (1380 MPa), d is the fiber diameter (20 μm), and τ is assumed to be equal to the shear yield strength of the matrix (~40 MPa). The strong fiber/matrix interface also reduces the length on either side of the broken fiber over which the matrix deforms plastically (see Cooper and Kelly 1967). For unidirectional composites with $V_f = 34\%$ and matrix tensile strength of 160 MPa, this length is only 0.04 mm. Therefore, plastic deformation is severely restricted in the unidirectional system, and the lack of fiber pull-out and the limited plastic deformation in the matrix are responsible for the planar fracture and the low γ_f.

In three-dimensional braided composites, fibers are not uniformly distributed in the matrix as in the unidirectional laminae, and each fiber bundle can be regarded as an individual reinforcement. The volume fraction of fibers within the bundle is approximately 50%, and the volume fraction of bundles in the composite is approximately 40%. Using the diameter of 2 mm and tensile strength of 586 MPa for the bundles, it is found that $l_c = 12.6$ mm and the length over which the matrix deforms plastically is 4 mm. Although factors such as fiber inclination and interactions among bundles are not considered above, these values illustrate the beneficial effect of fiber clustering on the extent of matrix plastic deformations and on the pull-out and debonding mechanisms. The non-homogeneous microstructure, therefore, appears to be at least partially responsible for the higher work of fracture of the three-dimensional braided composites as compared with the unidirectional laminate which shows a catastrophic planar fracture.

Majidi, Yang and Chou (1986) have also examined the effect of thermal treatment on the fiber/matrix interface strength and, hence, the fracture toughness of three-dimensional braided composites. The fiber/matrix interface deteriorates after isothermal heating at 500°C. There is a decrease in the fracture load and an increase in the amount of bundle pull-out which results in larger work of fracture ($\gamma_f = 20.30 \pm 14.35\ \text{kJ/m}^2$ after 72 hours of thermal treatment). This reflects the weak nature of the interfacial reaction zone which grows intergranularly towards the center of the fiber.

Guénon, Chou and Gillespie (1989) reported the in-plane fracture toughness, K_{Ic}, of carbon/epoxy composites with a three-dimensional orthogonal interlock fabric preform. The K_{Ic} values for three-dimensional fabric composites are $28.56\ \text{MPa}\sqrt{\text{m}}$ and $29.45\ \text{MPa}\sqrt{\text{m}}$ in two principal material directions, which are higher than that of laminates ($21.22\ \text{MPa}\sqrt{\text{m}}$). The through-the-thickness yarns are beneficial to the in-plane toughness by arresting and deviating the crack. The interaction between a crack and inhomogeneities, simulating fiber arrays, has been examined by Fowser and Chou (1989, 1990a&b).

7.7.3.2 *Interlaminar fracture*

Traditional laminated composites exhibit low interlaminar fracture toughness and are susceptible to delamination when subjected to interlaminar stress concentrations. Improvements in damage tolerance to date have focussed on utilizing tougher matrices (Hunston 1984) or interleafing concepts (Masters 1987). Through-the-thickness reinforcement provides an alternative approach to substantially increasing the resistance to delamination (see Whitney, Browning and Hoogsteden 1982; Guess and Reedy 1985; Mignery, Tan and Sun 1985; Dexter and Funk 1986; Fowser 1986; Guénon, Chou and Gillespie 1987; Ogo 1987).

The orthogonal interlock fabric architecture (Fig. 7.10) retains the in-plane performance while enhancing out-of-plane properties, by including a small amount of through-the-thickness reinforcement. The 'z direction' fibers are also known to be detrimental to the in-plane tensile and compressive properties. The interlocking process avoids the cutting of fibers, as it occurs in the stitching process. However, it creates matrix pockets that reduce the volume fraction of the in-plane fibers relative to the analogous two-dimensional laminates. The z direction fibers also tend to be deformed in the processing of the fabric composites.

Guénon, Chou and Gillespie (1989) have studied the effect of fiber geometry on the interlaminar and in-plane fracture behavior of

orthogonal interlocked fabric composites. The experimental work is based upon a T300/3501-6 carbon/epoxy system. Referring to Fig. 7.10, the fabric preform can be described as a [0°/90°] laminate in which some through-the-thickness yarns are interlaced. The in-plane yarns contain 6000 filaments per yarn and the through-the-thickness yarns have 1000 filaments per yarn. The spacing between two z direction yarns in both plate directions is 2.8 mm and the plate contains about 13 z direction yarns/cm^2. The total number of plies is 27, with 14 and 13 plies in two mutually orthogonal directions. The overall volume fraction is 50%, while the volume fraction of the z direction is 1%.

(A) Mode I interlaminar fracture

Guénon, Chou and Gillespie (1989) have adopted two test methods for Mode I interlaminar fracture, the double cantilever beam (DCB) test and the 'tabbed DCB', which uses long aluminum tabs bonded along both sides of the specimen to prevent the deviation of crack propagation from a self-similar manner. Both types of specimens are pin-loaded in tension in displacement-controlled mode.

The load–deflection curves for the three-dimensional composite specimens show a nonlinear unloading sequence and an appreciable permanent deformation after unloading. The crack tip did not completely close after unloading. These features can be explained by the crack closure process of the three-dimensional fabric composite. Most of the z direction yarns do not break in the plane of the crack. Instead, they fracture near the outer surface of the specimen where they are curved by the weaving process, and then debonded and pulled out. Figure 7.48 shows the fracture surface with the z direction yarn protruding out of the plane of fracture. During unloading, the pulled-out yarns do not resume their initial locations and therefore progressively undergo compressive stresses that lead to a nonlinear unloading behavior and a permanent deflection of the specimen after a zero load is reached.

Two data reduction methods have been adopted by Guénon, Chou and Gillespie (1989) for the three-dimensional fabric composites. These are the area method, based upon energy considerations, and the compliance method, based upon the linear elastic beam theory. The interlaminar critical strain energy release rate, G_{Ic}, values from the area method are 0.307 kJ/m^2 (two-dimensional regular DCB), 0.286 kJ/m^2 (two-dimensional tabbed DCB) and 3.85 kJ/m^2 (three-dimensional tabbed DCB). The compliance

method gives G_{Ic} values of 0.235 kJ/m^2 (two-dimensional regular DCB), 0.179 kJ/m^2 (two-dimensional tabbed DCB) and 2.66 kJ/m^2 (three-dimensional tabbed DCB). The compliance method only takes into account the energy of crack initiation. In the case of two-dimensional unidirectional laminates, the crack propagation energy is generally equal to the initiation energy and therefore both methods give similar results. In three-dimensional fabric composites, the fracture, debonding and pull-out of z direction yarns as well as the bridging of the crack by the z direction yarns dissipate energy. Therefore, the area method gives a higher and more accurate result of interlaminar fracture toughness.

The mode I delamination problem of three-dimensional orthogonal interlock fabric composites has been further examined by Byun, Gillespie and Chou (1990b) using a finite element analysis. The material systems and specimen geometries including two-dimensional regular DCB, two-dimensional tabbed DCB and three-dimensional tabbed DCB (see Guénon, Chou and Gillespie 1989) are simulated in this numerical work. Specifically, the mode I fracture behavior of carbon/epoxy composites is examined for

Fig. 7.48. Fracture surface of the orthogonal interlock fabric composite showing a pulled-out yarn. (After Guénon, Chou and Gillespie 1989.)

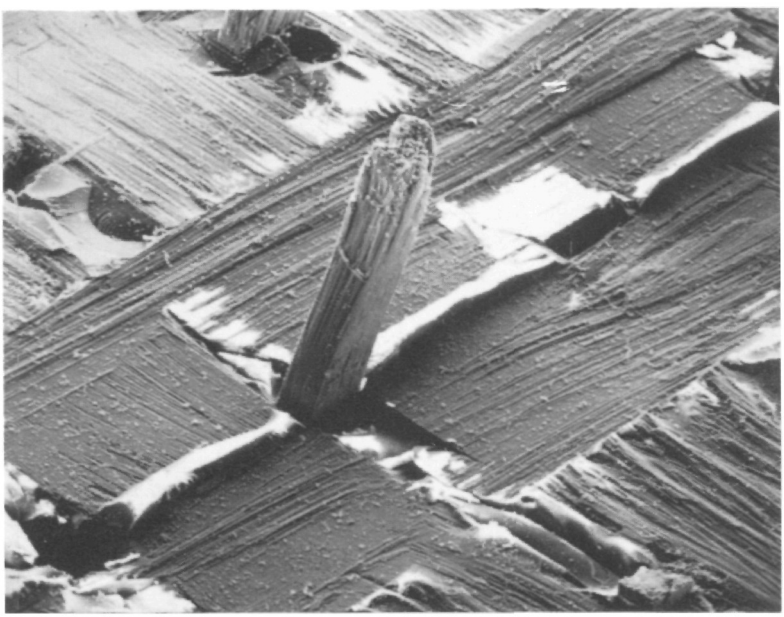

various initial crack lengths. The strain energy release rates, G_I, are evaluated based upon the crack closure method (Rybicki and Kanninen 1977) to ascertain the influence of through-the-thickness fibers on crack driving force. Byun and colleagues also have considered the effect of progressive debonding of the z axis yarns on the strain-energy release rate.

In the finite element model, the length of an element side is the crack increment utilized in the study ($\Delta a = 0.5562$ mm). The initial crack length is 25.4 mm and the locations of the through-the-thickness fibers are $3\Delta a$, $8\Delta a$, $13\Delta a$ and $18\Delta a$. A vertical unit displacement of 1 mm is applied to simulate the displacement controlled loading conditions used in the experimental work of Guénon and colleagues. Three types of through-the-thickness fiber debonding are modeled: perfect bonding, moderate bonding, where the z axis fiber is debonded over 25% of the specimen thickness, and complete debonding, where the load is carried by the fibers only. The z axis yarns are assumed to be initially perfectly bonded; partial or complete debonding does not occur until the crack front passes the reinforcement. Also, fiber fracture is not considered by Byun and colleagues.

Figure 7.49 demonstrates the effect of through-the-thickness yarns and bonding conditions on the strain-energy release rate. The strain-energy release rate for the two-dimensional laminate monotonically decreases with increasing crack length as one would expect

Fig. 7.49. Numerical strain-energy release rates of two-dimensional laminated and three-dimensional orthogonal woven composites as functions of crack length: — two-dimensional laminate; ○ fully debonded; + moderately bonded; ● perfectly bonded. (After Byun, Gillespie and Chou 1990.)

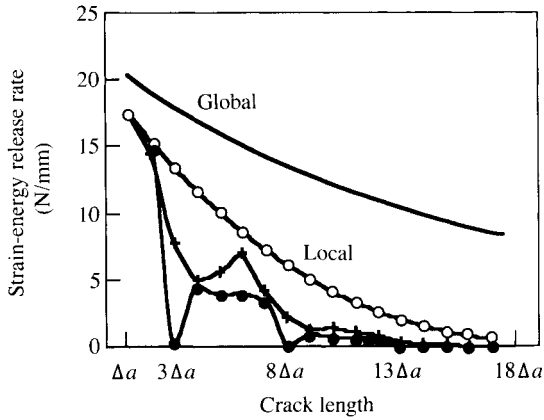

under fixed grip conditions. The introduction of through-the-thickness yarns reduces the local strain-energy release rate significantly in the case of perfect bonding condition as the crack approaches the first array of z axis yarns at $3\Delta a$. The crack driving force for interlaminar crack growth decreases because the load is transferred to the z axis yarns. The crack opening displacement is also reduced by the presence of the vertical fibers. As debonding occurs, the decrease of strain-energy release rate is less significant because the crack tip opening displacement increases.

In the numerical analysis, Byun and colleagues assume that the crack continues to propagate without fiber fracture. Consider the perfect bonding case of Fig. 7.49 when the crack propagates beyond the first array of yarns to $4\Delta a$. The strain-energy release rate is observed to increase slightly but is still significantly less than the two-dimensional specimen. This is due to the increase in deformation of the z axis yarns as load transfer occurs, which results in an increase in the crack tip opening displacement. Due to the presence of the z axis yarns at $8\Delta a$, the strain-energy release rate begins to diminish as the crack tip approaches the next site of through-the-thickness fibers where a second reduction in crack driving force is observed. The process continues until the strain-energy release rate is identically zero.

Figure 7.50 shows the tensile stress in the through-the-thickness yarn as a function of crack length. As the crack approaches the first yarn at $3\Delta a$, the load in the fiber increases rapidly. Additional crack

Fig. 7.50. Tensile stresses in the z axis fiber arrays as functions of crack length for perfect fiber–matrix bonding: — first array; ○ second array; ● third array (After Byun, Gillespie and Chou 1990.)

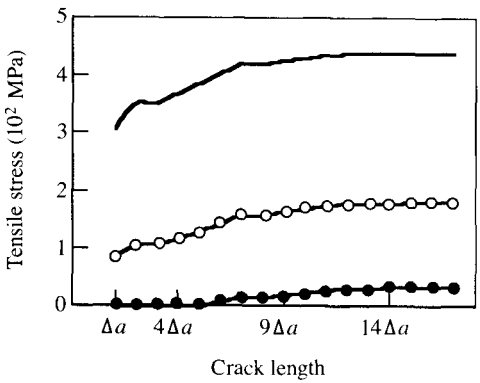

growth results in an asymptotic value of load in the first yarn as the second yarn begins to carry load. The process continues until the stress in the next array of yarns is zero. At this point, the applied load is being carried exclusively by multiple z axis yarns bridging the crack surface and the crack driving force is identically zero. The information presented in Figs. 7.49 and 7.50 demonstrates the load bearing and transferring mechanisms in the interlaminar fracture process of a three-dimensional fabric composite. This information enabled Byun and colleagues to predict the macroscopic critical load for mode I interlaminar fracture. More importantly, understanding of the load redistribution at the microscopic level is beneficial to the design of fabric preform structure for enhanced damage tolerance.

(B) Mode II interlaminar fracture

The mode II interlaminar fracture toughness of three-dimensional orthogonal fabric composite has been assessed by Liu and Chou (1989). The mode II fracture toughness tests are performed on both three-dimensional composites and two-dimensional laminates of the same carbon/epoxy system using end-notch-flexural (ENF) specimens.

Byun, Gillespie and Chou (1989), following the work of Liu and Chou (1989), have conducted a finite element analysis for evaluating the mode II strain-energy release rate. Similar to the mode I interlaminar fracture, the crack driving force for mode II interlaminar crack growth decreases as the crack approaches the z axis yarns because the load is being transferred to these yarns.

7.7.4 *Impact*

Majidi and Chou (1986) reported the impact behavior of both three-dimensional braided and unidirectional FP/Al–Li composites. The average fiber volume fractions are 17% and 34% for three-dimensional braided and unidirectional composites, respectively. Instrumented drop-weight impact tests have been carried out on un-notched impact panels, which do not require machining and, hence, do not sustain damage to the integrated fiber structure. Figure 7.51 compares the load–deflection traces obtained from through-the-thickness penetration impact tests. The three-dimensional braided composites absorb significantly higher energy and show larger deflection than the unidirectional composite during both damage initiation and propagation stages. By definition, the initiation energy is the area under the load–deflection curve up to

Fig. 7.51. Load–deflection traces obtained from through-the-thickness penetration impact tests. (a) Al–Li alloy; (b) three-dimensional braided FP/Al–Li composite; (c) unidirectional FP/Al–Li composite. (After Majidi and Chou 1986.)

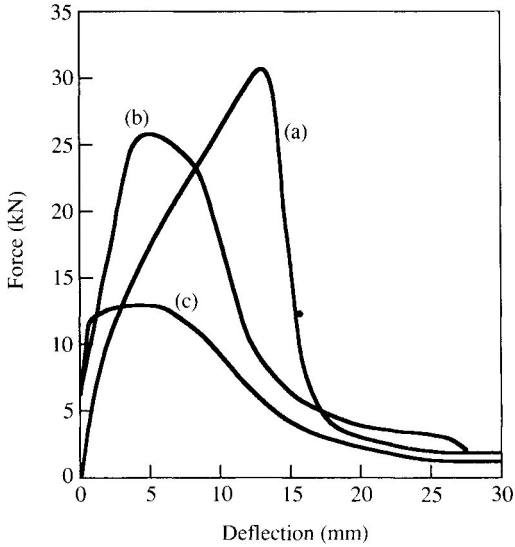

Fig. 7.52. Cross-sectional views of the FP/Al–Li composite specimens impacted at 54 J of incident energy. (a) Three-dimensional braided, $V_f = 0.17$; (b) three-dimensional braided, $V_f = 0.36$; (c) [±20°] angle-ply; (d) unidirectional laminate. (After Majidi and Chou 1987.)

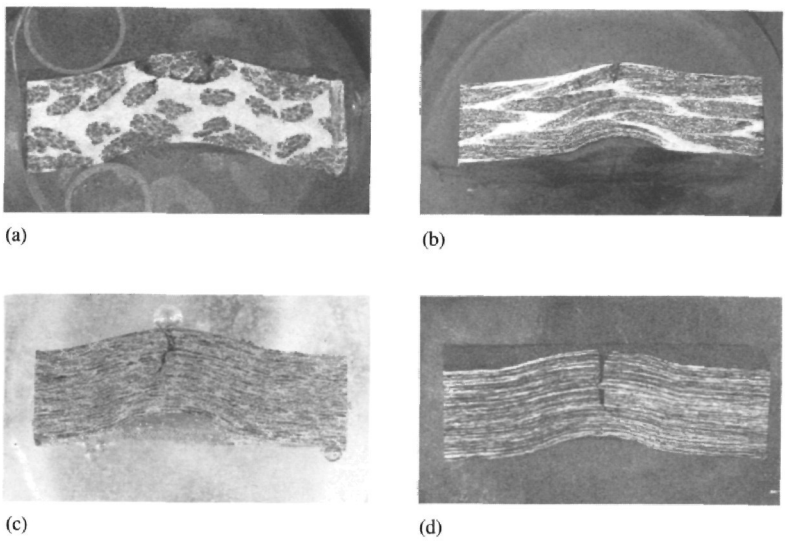

the maximum load. The total impact energy absorbed by the three-dimensional braided composites is close to that of the matrix material. The unidirectional composite fractures like a brittle material with cracks propagating through the entire specimen, while in the braided composite damage is restricted to a small region, and the specimen shows a ductile type of behavior. A comparison of the cross-sectional views of the FP/Al–Li composite specimen impacted at 54 J of incident energy is shown in Fig. 7.52.

Additional information on the mechanical behavior of three-dimensional fabric composites can be found in the work of Kregers and Teters (1982), Ko and Pastore (1985), Crane and Camponeschi (1986), Ko (1986), Yau, Ko and Chou (1986), Simonds, Stinchcomb and Jones (1988), Ko (1989b), and Whitcomb (1989).